RSC Advances

PAPER

View Article Online
View Journal | View Issue

Cite this: *RSC Adv.*, 2025, **15**, 6241

Mechanistic pathway and optimization of rhodamine B degradation using Mn_3O_4/ZnO nanocomposite on microalgae-based carbon

Hoc Thang Nguyen,[a] Van-Dat Doan,[b] Thi Lan Huong Nguyen,[c] Anh-Tien Nguyen,[d] Quang- Hieu Tran,[e] Vy Anh Tran*[f] and Van Thuan Le*[gh]

The development of cost-effective and eco-friendly photocatalysts for wastewater treatment is crucial for addressing environmental pollution challenges. In this study, we report a novel Mn_3O_4/ZnO nanocomposite supported on microalgae-derived activated carbon (AC) for the efficient photocatalytic degradation of rhodamine B (RhB) under visible light. FTIR analysis suggested interactions between the metal oxides and AC, while UV-vis DRS and PL studies revealed a reduced band gap and enhanced charge transfer in the composite, minimizing electron–hole recombination. The Mn_3O_4/ZnO/AC composite exhibited over 95.85% RhB removal efficiency and 80.56% mineralization after 420 min of irradiation. Stability tests showed over 88% degradation efficiency after four cycles, with no significant structural changes, as confirmed by XRD and SEM. Leaching tests demonstrated low Zn^{2+} (0.88 mg L^{-1}) and Mn^{2+} (0.26 mg L^{-1}) concentrations, well within WHO limits, indicating the composite's safety and structural integrity. Mechanistic studies identified hydroxyl and superoxide radicals as the main reactive species responsible for RhB degradation, with pathway analysis revealing the stepwise breakdown of the dye. This work highlights the potential of microalgae-derived AC as a sustainable support for photocatalysts, positioning the Mn_3O_4/ZnO/AC composite as a promising candidate for scalable wastewater treatment applications. The integration of green synthesis, high photocatalytic efficiency, and excellent safety profiles positions this composite as a valuable candidate for environmental remediation applications.

Received 26th January 2025
Accepted 20th February 2025

DOI: 10.1039/d5ra00625b

rsc.li/rsc-advances

1. Introduction

Water pollution is a critical environmental issue, intensified by industrial activities that discharge various contaminants into aquatic ecosystems. Among them, synthetic dyes, particularly rhodamine B (RhB), pose significant ecological and health risks due to their chemical stability and resistance to degradation. RhB, a cationic xanthene dye widely used in textiles, printing, and coatings, is known for its persistence in wastewater and potential carcinogenic effects.[1] Its removal from water bodies remains a pressing challenge, necessitating the development of efficient and sustainable treatment methods.

Photocatalysis has gained significant attention as a sustainable approach for eliminating organic pollutants under mild conditions while minimizing secondary pollution.[2] Zinc oxide (ZnO) is a widely studied photocatalyst due to its tunable band gap and high exciton binding energy.[3] However, its wide band gap (3.37 eV) restricts absorption primarily to the ultraviolet (UV) region, limiting its practical application.[4] To enhance its photocatalytic efficiency, ZnO is frequently modified through metal doping or heterojunction formation with other semiconductors.[5–7]

Recently, manganese oxide (Mn_3O_4), an emerging p-type semiconductor, has gained attention for its significant photocatalytic properties, effectively degrading various inorganic and organic pollutants in water. Its effectiveness is further enhanced when combined with other metal oxides, where it contributes to improved catalytic activity through synergetic effects. Moreover, Mn_3O_4 is economical, non-toxic, and can be synthesized using simple protocols, making it an attractive and sustainable choice for environmental remediation applications.[8] The previous

[a]*Faculty of Chemical Technology, Ho Chi Minh City University of Industry and Trade, 140 Le Trong Tan, Ho Chi Minh City, 700000, Vietnam*
[b]*Faculty of Chemical Engineering, Industrial University of Ho Chi Minh City, Ho Chi Minh City, 700000, Vietnam*
[c]*Institute of Biotechnology and Food Technology, Industrial University of Ho Chi Minh City, Ho Chi Minh City, 700000, Vietnam*
[d]*Faculty of Chemistry, Ho Chi Minh City University of Education, 280 An Duong Vuong, Ho Chi Minh City, 700000, Vietnam*
[e]*Basic Sciences Department-Saigon Technology University, 180 Cao Lo, Ho Chi Minh City 700000, Vietnam*
[f]*Deparment of Material Science, Institute of Applied Technology and Sustainable Development, Nguyen Tat Thanh University, Ho Chi Minh City, 700000, Vietnam. E-mail: tavy@ntt.edu.vn*
[g]*Center for Advanced Chemistry, Institute of Research & Development, Duy Tan University, 03 Quang Trung, Da Nang City, 550000, Vietnam. E-mail: levanthuan3@duytan.edu.vn*
[h]*Faculty of Natural Sciences, Duy Tan University, 03 Quang Trung, Da Nang City, 550000, Vietnam*

studies have demonstrated that the synergy between ZnO and Mn_3O_4 can enhance catalytic activity through improved surface area, facilitating the adsorption of pollutants and promoting the separation of photogenerated electron–hole pairs.[9] The hierarchical nanostructures formed by the Mn_3O_4/ZnO composite are expected to improve electron mobility and extend the light-harvesting range, leading to more efficient photocatalytic degradation of organic contaminants. Despite these advantages, practical application of Mn_3O_4/ZnO nanocomposites is hindered by issues such as nanoparticle aggregation and challenges in catalyst recovery. To address these limitations, carbon-based materials, particularly activated carbon (AC), have been integrated with photocatalysts to improve dispersion, enhance adsorption, and facilitate electron transfer due to its high surface area, tunable porosity, and eco-friendly nature.[10] In the search for sustainable and eco-friendly sources of AC, algae have emerged as a promising alternative. Several studies have highlighted the significant potential of algae-based AC in water treatment applications. For instance, Shoaib *et al.* utilized green algae *Ulva lactuca* to synthesize AC, achieving an impressive adsorption capacity of 303.78 mg g^{-1} for methylene blue dye from aqueous solutions.[11] Similarly, Djezzar *et al.* produced AC from the green algae *Spirogyra* utilized it as an economical adsorbent for efficiently capturing copper(II) ions in industrial wastewater treatment.[12] Additionally, the presence of nitrogen-functional groups in algae-based AC has also been shown to improve its surface chemistry and adsorption capacity, further enhancing its effectiveness as a pollutant adsorbent.[11] These findings underscore the potential of using algae-derived AC, especially when modified, in environmental remediation applications.

In this study, we synthesized and characterized a novel Mn_3O_4/ZnO nanocomposite supported on microalgae-derived AC (Mn_3O_4/ZnO/AC) for the photocatalytic degradation of RhB. This composite aims to leverage the synergistic effects of ZnO and Mn_3O_4 while utilizing algae-derived AC to enhance stability and adsorption capabilities. Although Mn_3O_4/ZnO composites have been explored, the integration of algae-derived AC as a support material has not been reported. This study pioneers a novel Mn_3O_4/ZnO/AC nanocomposite, aiming to leverage the synergistic effects of ZnO, Mn_3O_4, and AC for enhanced photocatalytic activity and catalyst stability. The photocatalytic performance of Mn_3O_4/ZnO/AC was systematically evaluated under varying conditions, including catalyst dosage, pH, temperature, and dye concentration. Additionally, catalyst reusability and stability were assessed to determine its potential for practical water treatment applications.

2. Materials and methods

2.1. Materials and equipment

In this study, various chemicals were utilized for material synthesis, photocatalytic experiments, and scavenger tests. Zinc acetate dihydrate ($Zn(CH_3COO)_2 \cdot 2H_2O$, 99.5%) and manganese(II) chloride tetrahydrate ($MnCl_2 \cdot 4H_2O$, ≥98%) were employed as precursor materials for catalyst synthesis. Rhodamine B ($C_{28}H_{31}ClN_2O_3$, 90%) served as the model organic pollutant to evaluate photocatalytic performance. For pH adjustment, hydrochloric acid (HCl, 37%) and sodium hydroxide (NaOH, ≥98.0%) were used. In the scavenger study, sodium formate (HCOONa, ≥99.0%), potassium dichromate ($K_2Cr_2O_7$, ≥99.5%), *p*-benzoquinone (*p*-BQ, $C_6H_4(=O)_2$, ≥98%), and isopropanol (IPA, $(CH_3)_2CHOH$, ≥98%) were employed to identify reactive species. Additional reagents, including ammonium chloride (NH_4Cl, ≥99.5%), hydrogen peroxide (H_2O_2, 30%), aqueous ammonia solution (NH_3, 30%), and ethanol (C_2H_5OH, 99.7%), were used in the synthesis and experimental processes. All chemicals were purchased from Sigma-Aldrich and used as received without further purification. The green microalgae (*Chlamydomonas reinhardtii*) used as the precursor for AC were collected from a fish pond in Bến Tre Province, Vietnam. After collection, the algae underwent thorough washing and screening to remove impurities, resulting in a pure culture of green microalgae for further experimentation.

For the characterization of the synthesized materials, several instruments were utilized. UV-vis absorption spectra were recorded using a Metash UV-vis 5100 spectrophotometer, while FT-IR spectra were obtained with a Tensor 27 spectrometer from Bruker, Germany. The crystalline structures of the samples were analyzed using a Shimadzu 6100 X-ray diffractometer (XRD). The UV-vis diffuse reflectance spectra (DRS) were measured using a Cary 4000 Eclipse Fluorescence Spectrometer (Agilent, USA). The morphology and detailed structure of the samples were examined using field emission scanning electron microscopy (FE-SEM) with a model S-4800 and high-resolution transmission electron microscopy (HR-TEM) with a JEM 2100 from JEOL (Japan). The elemental composition was determined by energy-dispersive X-ray spectroscopy (EDX) using an S-4800 FE-SEM. Photoluminescence (PL) spectra were also recorded using the Cary 4000 Eclipse Fluorescence Spectrometer. Additionally, the specific surface area and porosity of the samples were analyzed using a NOVA 1200e surface area analyzer (Quantachrome Instruments, USA). The degree of contaminant mineralization was assessed by determining the total organic carbon (TOC) content with a Multi N/S 2100S TOC analyzer (Analytik Jena, Germany). The identification and analysis of organic intermediates and byproducts generated during the reaction were conducted using gas chromatography-mass spectrometry (GC-MS) on an Agilent 7890A/5975C system (USA). To evaluate the leaching of Zn and Mn ions throughout the photocatalytic process, inductively coupled plasma mass spectrometry (ICP-MS) was carried out on an Agilent 7700 series instrument (USA), ensuring accurate quantification of metal ion release and providing valuable information on the catalyst's stability over time.

2.2. Synthesis of catalyst materials

2.2.1. Synthesis of AC from green microalgae. The collected green microalgae were thoroughly washed and treated with 1 M H_2SO_4 to adjust the pH to 2, which facilitated the breakdown of cellulose. The mixture was stirred for 15 min, followed by neutralization using 1 M NaOH until the pH reached 7. The treated algae were then filtered and washed with distilled water.

The resulting biomass was subjected to a hydrothermal process in an autoclave at 200 °C for 2 h. The resulting AC was washed with ethanol and distilled water and then dried at 60 °C to remove any residual solvents.

2.2.2. Synthesis of ZnO/AC composite. To prepare the ZnO/AC composite, 0.03 g of the synthesized AC was dispersed in 20 mL of distilled water and subjected to sonication for 30 min to achieve a homogenous suspension (Solution A). Separately, 0.84 g of $Zn(CH_3COO)_2 \cdot 2H_2O$ was dissolved in 20 mL of distilled water, followed by the addition of 5 mL of 1 M NaOH solution with continuous stirring for 5 min, resulting in Solution B. Solution A was then added dropwise to Solution B under sonication for an additional 15 min. Subsequently, 5 mL of 30% H_2O_2 was slowly added to the mixture. The formation of a white precipitate, which consisted of ZnO and $Zn(OH)_2$, was observed. The precipitate was filtered and washed with ethanol, then heated at 90 °C for 15 min to ensure the complete conversion of $Zn(OH)_2$ to ZnO. The ZnO/AC composite was then washed with distilled water and dried at 60 °C.

2.2.3. Preparation of Mn_3O_4 nanoparticles. Mn_3O_4 nanoparticles were synthesized by dissolving 6 g of $MnCl_2 \cdot 4H_2O$ in 50 mL of distilled water. To this solution, 8 mL of ammonia solution (30%) was added, resulting in the formation of a white precipitate of $Mn(OH)_2$. Separately, 4 g of NH_4Cl was dissolved in 20 mL of deionized water and added to the $Mn(OH)_2$ suspension. This caused the precipitate to dissolve, and the solution turned light red, indicating the formation of a soluble manganese complex. Oxygen was then bubbled through the solution at a rate of 1.5 L min^{-1}, promoting the slow precipitation of Mn_3O_4. The Mn_3O_4 precipitate was then filtered, washed with distilled water, and dried at 60 °C.

2.2.4. Synthesis of Mn_3O_4/ZnO/AC composite. The Mn_3O_4/ZnO/AC composite was synthesized by first dispersing 0.03 g of the synthesized Mn_3O_4 nanoparticles in 20 mL of distilled water in Beaker A, followed by sonication for 30 min. Simultaneously, 0.30 g of the ZnO/AC composite was dispersed in 50 mL of distilled water in Beaker B and sonicated for 30 min. Once both suspensions were fully dispersed, the contents of Beaker A were slowly added to Beaker B under continuous sonication for an additional 15 min. The resulting solid was filtered, washed with ethanol, and dried at 60 °C. The synthesis procedure of Mn_3O_4/ZnO/AC composite is summarized in Scheme 1.

2.2.5. Synthesis of ZnO and Mn_3O_4/AC. For comparative purposes, pure ZnO and Mn_3O_4/AC were also synthesized. Pure ZnO was prepared by dissolving 0.84 g of $Zn(CH_3COO)_2 \cdot 2H_2O$ in 20 mL of distilled water. Afterward, 5 mL of 1 M NaOH solution was added with continuous stirring for 5 min, resulting in the formation of a white precipitate of $Zn(OH)_2$. To achieve full conversion to ZnO, the precipitate was collected by filtration, rinsed with ethanol, and subsequently heated at 90 °C for 15 min. The product was washed with distilled water and dried at 60 °C. Meanwhile, Mn_3O_4/AC was synthesized by mixing 0.3 g of Mn_3O_4 with 0.3 g of AC in 50 mL of distilled water, followed by sonication for 1 h. The resulting solid was filtered, dried, and heated at 60 °C for 30 min to obtain Mn_3O_4/AC.

2.3. Catalytic study

The catalytic performance of the synthesized Mn_3O_4/ZnO/AC composite was evaluated through the degradation of RhB under visible light irradiation. The experiments were designed to investigate the effects of catalyst dosage, pH, RhB concentration, temperature, and the presence of radical scavengers on the degradation efficiency, as well as the catalyst's reusability. The photocatalytic activity was assessed by monitoring the degradation of RhB in an aqueous solution. In a typical experiment, 100 mg of the Mn_3O_4/ZnO/AC catalyst was dispersed in 50 mL of 10 mg L^{-1} RhB solution. To ensure adsorption–desorption equilibrium between RhB and the catalyst, the suspension was stirred in the dark for 1 hour before initiating the photocatalytic reaction. Afterward, the solution was irradiated using a 250 W Xenon lamp equipped with a UV cutoff filter (λ > 420 nm) to ensure visible light irradiation. During irradiation, 2–3 mL aliquots of the suspension were withdrawn at 30 minute intervals. The aliquots were centrifuged to remove the catalyst particles, and the remaining RhB concentration was measured using UV-vis spectrophotometry at 553 nm, which corresponds to the characteristic absorption peak of RhB.

The removal efficiency, mineralization rate, and degradation kinetics were calculated using eqn (1)–(3), respectively:

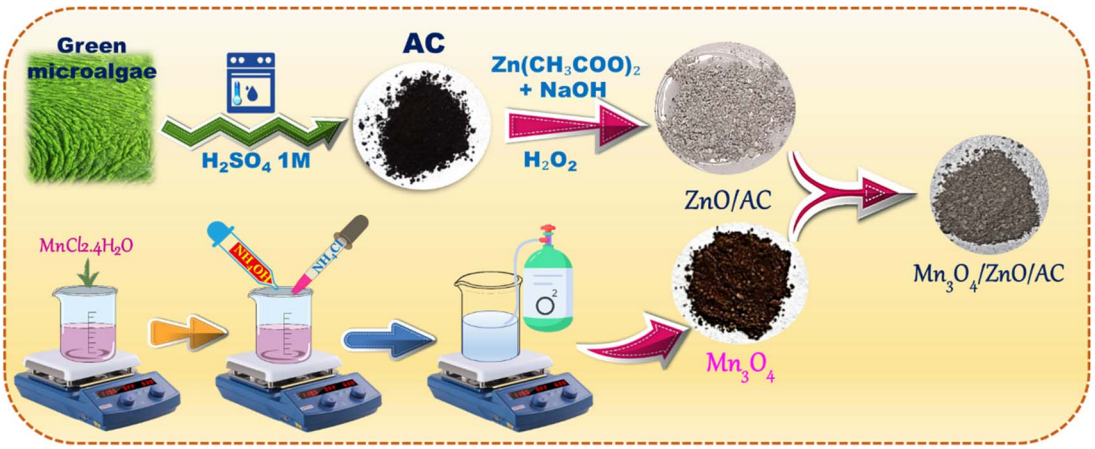

Scheme 1 The synthesis procedure of Mn_3O_4/ZnO/AG composite.

$$\text{removal efficiency } (\%) = \frac{C_0 - C_t}{C_0} \times 100 \quad (1)$$

$$\text{mineralization } (\%) = \frac{\text{TOC}_{\text{initial}} - \text{TOC}_{\text{final}}}{\text{TOC}_{\text{initial}}} \times 100 \quad (2)$$

$$\text{pseudo-first-order kinetic model : } -\ln\left(\frac{C_t}{C_0}\right) = kt \quad (3)$$

in these equations, C_0 and C_t denote the initial concentration of RhB and its concentration at time t, respectively; $\text{TOC}_{\text{initial}}$ and $\text{TOC}_{\text{final}}$ denote the initial and final TOC values; and k is the pseudo-first-order rate constant.

The effect of catalyst dosage on the degradation efficiency was studied by varying the amount of Mn_3O_4/ZnO/AC in the reaction mixture. Experiments were conducted with catalyst dosages of 0.05 g, 0.075 g, 0.1 g, and 0.125 g, using 50 mL of 10 mg L^{-1} RhB solution. The reaction conditions, including stirring at 200 rpm and room temperature, were kept constant. Post-reaction, the remaining RhB concentration was determined as described above. The relationship between catalyst dosage and degradation efficiency was plotted to identify the optimal catalyst amount for maximum degradation. The degradation efficiency was also evaluated across different pH levels to determine the optimal pH for RhB degradation. The pH of the RhB solution (10 mg L^{-1}) was adjusted to pH 3, 5, 7, 9, and 11 using either HCl or NaOH before adding the catalyst. The same photocatalytic procedure was followed, and the degradation efficiency was calculated to assess the influence of pH on the catalyst's performance. The impact of initial RhB concentration on the degradation efficiency was investigated by preparing RhB solutions with concentrations of 5, 10, 15, and 20 mg L^{-1}. The catalyst dosage was fixed at the optimal amount determined from previous experiments. The degradation process was monitored, and the efficiency was calculated for each concentration to determine the concentration that results in the highest degradation rate. The influence of temperature on the photocatalytic activity was examined by performing the degradation reactions at different temperatures: 25 °C, 35 °C, and 45 °C. The catalyst dosage and RhB concentration were kept constant, and the degradation efficiency was monitored to evaluate the effect of temperature on the reaction kinetics.

To identify the active species involved in the degradation process, experiments were conducted in the presence of different radical scavengers. *p*-BQ for superoxide radicals ($^{\bullet}O_2^-$), IPA for hydroxyl radicals ($^{\bullet}OH$), HCOONa for holes (h^+), and $K_2Cr_2O_7$ for electrons (e^-) were added to the reaction mixture at a concentration of 10 mM. The impact of each scavenger on the degradation efficiency was analyzed to elucidate the mechanism of RhB degradation by the Mn_3O_4/ZnO/AC catalyst.

The reusability of the Mn_3O_4/ZnO/AC catalyst was assessed over four consecutive cycles of RhB degradation under the same conditions. After each cycle, the catalyst was recovered by centrifugation, washed with ethanol and distilled water, and dried at 60 °C before being reused. The degradation efficiency was measured after each cycle to evaluate the stability and reusability of the catalyst. All experiments were repeated independently three times, and the results are presented as the mean with standard deviation to ensure accuracy and reliability. Error bars are included in all figures to represent the variation across the different trials.

3. Results and discussion

3.1. Characterization of catalysts

3.1.1. XRD analysis. Fig. 1a shows the XRD patterns of the samples: AC derived from green microalgae, Mn_3O_4, ZnO, and the Mn_3O_4/ZnO/AC nanocomposite. The XRD pattern of AC exhibits a broad and weak peak around $2\theta \approx 24°$, which is characteristic of the amorphous structure of carbon. This peak is typically associated with the (002) plane of graphitic carbon.[13] However, due to the origin from green microalgae and the activation process, the structure of AC is not fully ordered, resulting in a broad and less distinct peak. This indicates that AC has a porous structure with numerous voids and defects, a key feature for applications in adsorption and catalysis.[14] The XRD pattern of Mn_3O_4 displays sharp diffraction peaks at $2\theta \approx$ 17.9°, 28.8°, 32.3°, 36.1°, 38.0°, 44.5°, 50.7°, 58.5°, 59.8° and 64.7°, corresponding to the (101), (112), (103), (211), (004), (220), (105), (321), (244), and (400) planes of the spinel Mn_3O_4 structure (JCPDS no. 24-0734).[15] The presence of these sharp and

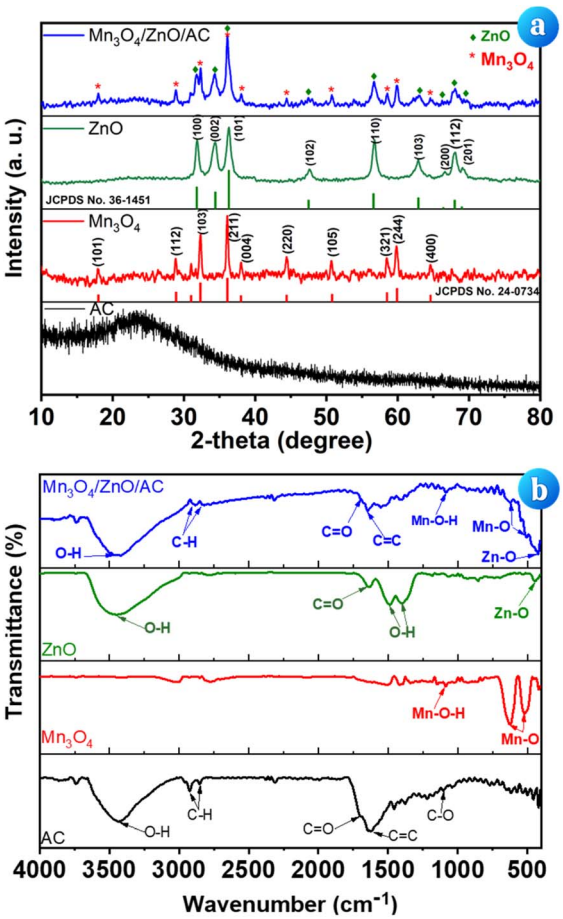

Fig. 1 XRD patterns (a) and FTIR spectra (b) of AC, Mn_3O_4, ZnO, and Mn_3O_4/ZnO/AC composite.

intense peaks indicates that Mn_3O_4 possesses high crystallinity, which is often advantageous for catalytic activity, particularly in oxidation reactions. For ZnO, the XRD pattern shows characteristic peaks at $2\theta \approx 31.9°$, 34.4°, 36.3°, 47.7°, 56.8°, 62.9°, 66.7°, 68.1°, and 69.1°, corresponding to the (100), (002), (101), (102), (110), (103), (200), (112), and (201) planes of the wurtzite ZnO structure (JCPDS no. 36-1451). The sharp peaks in the ZnO pattern indicate that ZnO exists in a crystalline form with a high degree of order, which can provide effective active sites for photocatalytic reactions. The XRD pattern of the Mn_3O_4/ZnO/AC nanocomposite exhibits the characteristic diffraction peaks of both Mn_3O_4 and ZnO, but with slightly reduced intensity and sometimes broader peaks compared to the pure samples. The reduction in intensity and broadening of peaks could be attributed to strong interactions between Mn_3O_4, ZnO, and AC, or due to a reduction in crystallite size when combined with AC. Additionally, the presence of AC in the nanocomposite may act as a supporting matrix, improving the dispersion of Mn_3O_4 and ZnO particles and providing additional adsorption sites. This structure facilitates electron transfer during photocatalytic reactions, potentially leading to enhanced photocatalytic performance compared to the individual components.

The crystallite sizes (denoted as D (in nm)) of Mn_3O_4 and ZnO were estimated using the Scherrer equation (eqn (4)):

$$D = \frac{K\lambda}{\beta \cos \theta} \quad (4)$$

where K represents the shape factor, typically assumed to be 0.9 for spherical particles; λ is the wavelength of the X-ray used (0.15406 nm for Cu Kα radiation); β is the full width at half maximum of the diffraction peak (in radians); and θ is the Bragg angle of the peak. The calculated average crystallite sizes for pure Mn_3O_4 and ZnO were 28.58 nm and 12.11 nm, respectively. In the Mn_3O_4/ZnO/AC composite, the crystallite sizes of Mn_3O_4 and ZnO were determined to be 23.16 nm and 12.87 nm, respectively. The reduction in the Mn_3O_4 crystallite size suggests that the synthesis method, involving sonication and dispersion in the presence of ZnO/AC, facilitated a more homogeneous distribution of Mn_3O_4 nanoparticles. This improved dispersion likely enhances the interaction between Mn_3O_4 and the AC support, increasing the number of exposed active sites and potentially improving catalytic performance. In contrast, the crystallite size of ZnO in the composite remained nearly unchanged. This stability indicates that the ZnO/AC composite maintained its structural integrity during the synthesis process, further confirming the robustness of the ZnO/AC matrix as a support for Mn_3O_4 nanoparticles. The combination of Mn_3O_4, ZnO, and AC in this composite leverages the strengths of each component. AC provides a porous matrix for effective dispersion, ZnO contributes to the structural stability, and Mn_3O_4 introduces active catalytic sites. The tailored crystallite sizes ensure an optimized balance of surface area and crystallinity, crucial for photocatalytic and adsorption applications.

3.1.2. FTIR analysis. Fig. 1b illustrates the FTIR spectra of AC, ZnO, Mn_3O_4, and the Mn_3O_4/ZnO/AC composite. The spectra reveal important functional groups and bonds associated with each material, which provide insights into their structure and interactions. For AC, the broad absorption band centered around 3435 cm^{-1} is attributed to O–H stretching vibrations, signifying the presence of hydroxyl groups typically found on its surface. The peaks at 2928 cm^{-1} and 2852 cm^{-1} are associated with C–H stretching vibrations from aliphatic chains, likely due to surface-bound hydrocarbons. A peak at 1700 cm^{-1} is attributed to C=O stretching, characteristic of carbonyl groups, which may result from surface oxidation during the activation process. Peaks observed in the region of 1600–1650 cm^{-1} are assigned to C=C stretching vibrations, suggesting the presence of aromatic structures. Additionally, the peaks around 1100 cm^{-1} can be assigned to C–O stretching, likely from ether or ester functionalities.[16,17]

The FTIR spectrum of Mn_3O_4 displays several characteristic absorption bands corresponding to Mn–O vibrations, which are indicative of its spinel structure. Specifically, strong absorption bands are observed at 623 cm^{-1} and 521 cm^{-1}, which can be attributed to the stretching vibrations of Mn–O bonds in the tetrahedral and octahedral sites within the spinel lattice. Additionally, a weak band at 1086 cm^{-1} is observed, which may be attributed to Mn–O–H vibrations, likely due to surface hydroxylation or minor moisture absorption.[18] Peaks at 1400 cm^{-1} and 1480 cm^{-1} are attributed to various vibrational modes of O–H groups from adsorbed water on the ZnO surface. The peak at 1632 cm^{-1} is assigned to the asymmetric stretching vibration of C=O, indicative of CO_2 adsorption from ambient air. Finally, the broad absorption band near 3432 cm^{-1} is associated with O–H stretching vibrations, confirming the presence of adsorbed water, which is attributed to the hygroscopic nature of ZnO.[19]

For the Mn_3O_4/ZnO/AC composite, the FTIR spectrum shows a combination of features from its individual components. The broad O–H stretching band around 3440 cm^{-1}, which remains consistent with the intensity observed in pure AC, indicates the presence of hydroxyl groups. The Zn–O stretching band at approximately 430 cm^{-1} is still present, confirming the incorporation of ZnO into the composite. Additionally, the Mn–O stretching bands from Mn_3O_4 are evident in the region of 500–600 cm^{-1}, further verifying the presence of manganese oxide. The composite spectrum also shows a slight shift or broadening of the Zn–O and Mn–O peaks compared to the pure materials, suggesting possible interactions between Mn_3O_4, ZnO, and AC in the composite. These interactions may enhance the material's structural stability and photocatalytic properties by promoting better electron transfer and reducing recombination of electron–hole pairs during photocatalysis.

3.1.3. SEM, EDX and TEM studies. The SEM images in Fig. 2 provide an in-depth view of the surface morphology of the synthesized materials, complemented by EDX analysis and elemental mapping to confirm the elemental composition. Fig. 2a displays the SEM image of AC derived from green microalgae. The AC exhibits a porous and relatively uniform structure, with particle sizes ranging from approximately 300 to 800 nm. This size is significantly smaller compared to the green algae *Ulva lactuca* biochar-sulfur modified with H_2SO_4 and $NaHCO_3$, which has particle sizes between 1800 and 7884 nm.[11]

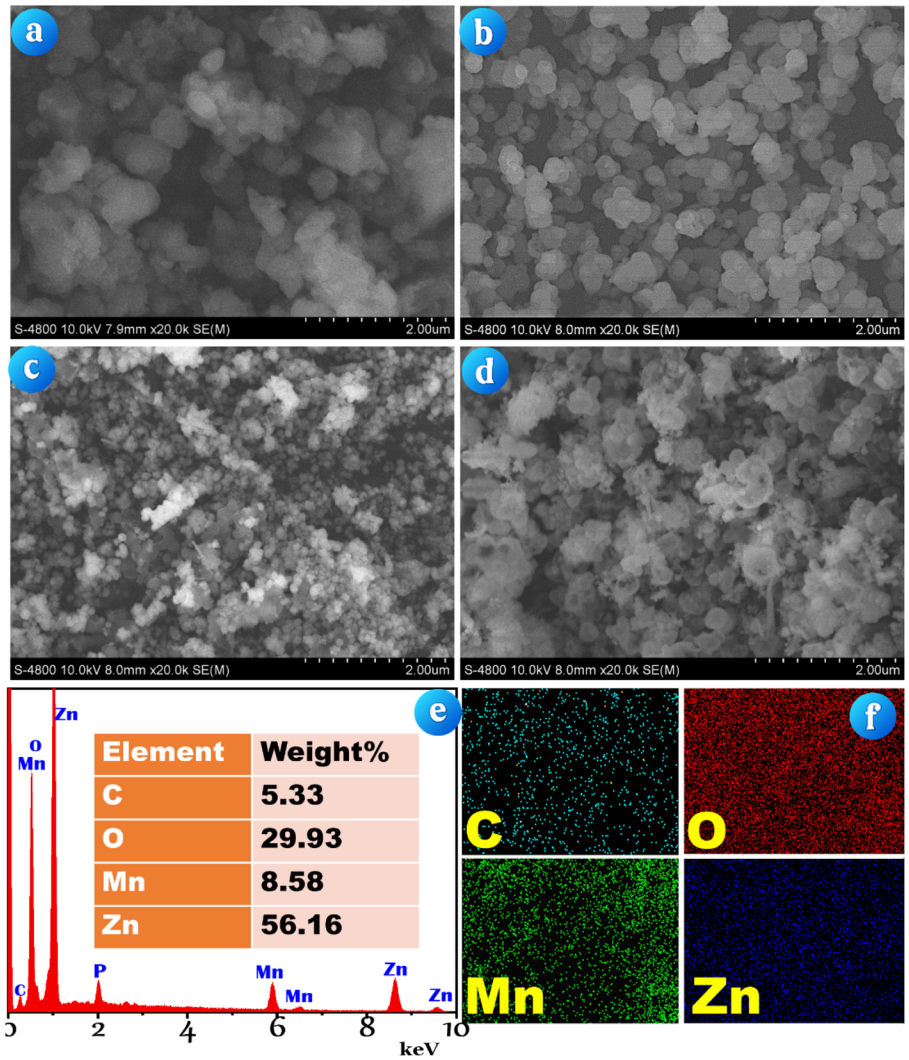

Fig. 2 SEM images of (a) AC derived from green microalgae, (b) ZnO/AC, (c) Mn_3O_4 and (d) Mn_3O_4/ZnO/AC composites; (e) EDX spectrum and (f) element mapping of the Mn_3O_4/ZnO/AC composite.

The smaller and more uniform particle size of the AC can be attributed to the use of microalgae with naturally smaller and more consistent dimensions. This uniformity, combined with the porosity of the material, is essential as it enhances the material's capacity to support metal oxides, potentially leading to improved catalytic properties. Fig. 2b shows the SEM image of the ZnO/AC composite, which maintains a morphology similar to that of the AC. The ZnO nanoparticles, synthesized *in situ* within the AC matrix, are not visible in this image, likely due to their very small size (below 10 nm). The uniform distribution of ZnO is inferred, and this observation is further validated by the TEM analysis presented in Fig. 3.

Fig. 2c presents the SEM image of Mn_3O_4, where the nanoparticles exhibit a spherical morphology with relatively uniform sizes, ranging from 100 to 200 nm. This consistency in particle size suggests a well-controlled synthesis process, which is critical for ensuring uniform catalytic activity. Fig. 2d captures the Mn_3O_4/ZnO/AC composite. The image reveals a complex structure where Mn_3O_4 and ZnO particles are dispersed within the AC matrix. The spherical Mn_3O_4 particles are clearly visible, while the ZnO particles remain too small to be detected by SEM, suggesting successful integration within the AC matrix.

The EDX spectrum in Fig. 2e complements the SEM images by confirming the elemental composition of the Mn_3O_4/ZnO/AC composite. Peaks corresponding to carbon (5.33%), oxygen (29.93%), manganese (8.58%), and zinc (56.16%) are clearly observed, indicating the successful incorporation of both Mn_3O_4 and ZnO onto the AC substrate. Additionally, a peak for phosphorus (P) is also detected, which is likely due to the inherent phosphorus content present in the microalgae. Fig. 2f provides elemental mapping images that visually represent the distribution of these elements within the composite. The uniform distribution of carbon, oxygen, manganese, and zinc throughout the material highlights the homogeneous integration of the active components, which is vital for consistent catalytic performance.

Further insights into the nanostructure of the ZnO/AC and Mn_3O_4/ZnO/AC composites are provided by the TEM images in Fig. 3. Fig. 3a shows the TEM image of the ZnO/AC composite, where ZnO nanoparticles are observed as small, evenly

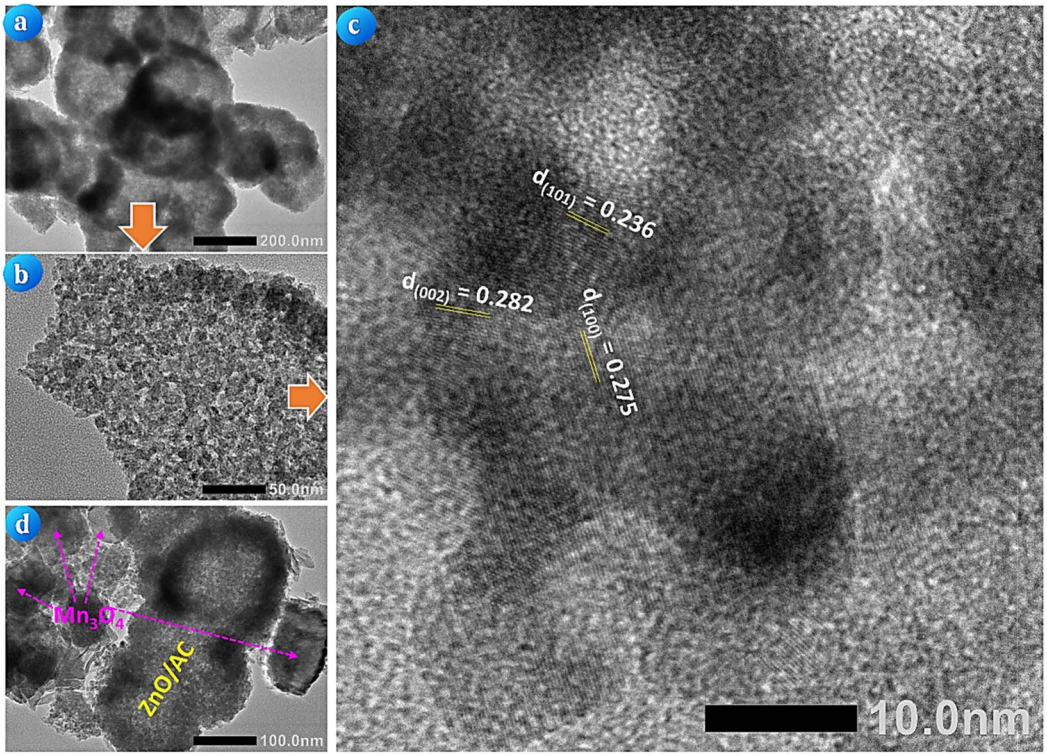

Fig. 3 (a) and (b) TEM images of ZnO/AC showing a porous AC structure with well-dispersed ZnO nanoparticles; (c) HRTEM image of ZnO/AC with *d*-spacings corresponding to ZnO crystallographic planes; (d) TEM image of Mn_3O_4/ZnO/AC.

distributed particles on the AC matrix. The small size of these nanoparticles, consistent with the *in situ* synthesis, contributes to a high surface area for catalytic reactions. Fig. 3b offers a higher-resolution TEM image of the ZnO/AC composite, confirming that ZnO nanoparticles are well-dispersed within the matrix. The particles range from 5 to 10 nm, explaining their invisibility in SEM images. Fig. 3c provides an HR-TEM image of the ZnO/AC composite, with clear lattice fringes corresponding to ZnO. The *d*-spacing values, including $d(101) = 0.236$ nm, $d(002) = 0.282$ nm, and $d(100) = 0.275$ nm, affirm the crystalline nature of ZnO and confirm its successful synthesis within the AC matrix.[20] Fig. 3d displays the TEM image of the Mn_3O_4/ZnO/AC composite, where spherical Mn_3O_4 particles are well-dispersed within the ZnO/AC matrix. The clear distinction between Mn_3O_4 and ZnO phases indicates that both materials are effectively integrated into the composite, enhancing its multifunctional catalytic properties.

3.1.4. Optical properties. The PL spectra of the samples, as presented in Fig. 4a, provide key insights into the charge recombination behavior of the Mn_3O_4/ZnO/AC nanocomposite compared to its individual components. The ZnO sample exhibits two distinct emission peaks at 484 nm and 545 nm. The peak at 484 nm is attributed to electronic transitions from zinc interstitial (Zn_i) sites to the valence band, while the peak at 545 nm is associated with the recombination of a photogenerated hole with singly ionized oxygen vacancies on the surface of the ZnO nanoparticles.[21] These defects can act as recombination centers for photogenerated electron–hole pairs, suggesting significant charge carrier recombination within the ZnO structure. The presence of these emission peaks indicates a relatively high rate of charge recombination, which typically limits the photocatalytic efficiency of pure ZnO.[22] In contrast, the PL intensity of the Mn_3O_4 sample is significantly lower, demonstrating that Mn_3O_4 possesses fewer surface defects and thus, exhibits reduced electron–hole recombination compared to ZnO. This reduced recombination is beneficial for photocatalytic applications, as it increases the availability of charge carriers for surface reactions. The AC sample shows negligible PL emission, reflecting its non-luminescent nature and minimal contribution to charge carrier recombination. This is consistent with the role of AC primarily as an adsorbent material, enhancing surface area and pollutant adsorption rather than participating in the photogenerated charge dynamics.

Most notably, the Mn_3O_4/ZnO/AC nanocomposite exhibits a significantly lower PL intensity compared to pure ZnO. This suggests that the incorporation of Mn_3O_4 and AC into the ZnO matrix effectively suppresses the recombination of electron–hole pairs. The reduction in PL intensity indicates enhanced charge separation within the composite, likely due to the synergistic interaction between Mn_3O_4 and ZnO, as well as the conductive properties of AC, which may facilitate electron transfer and further reduce recombination. Consequently, the Mn_3O_4/ZnO/AC composite is expected to exhibit superior photocatalytic performance compared to the individual components, as the lower PL intensity correlates with improved charge separation and a longer lifetime of the photogenerated charge carriers.

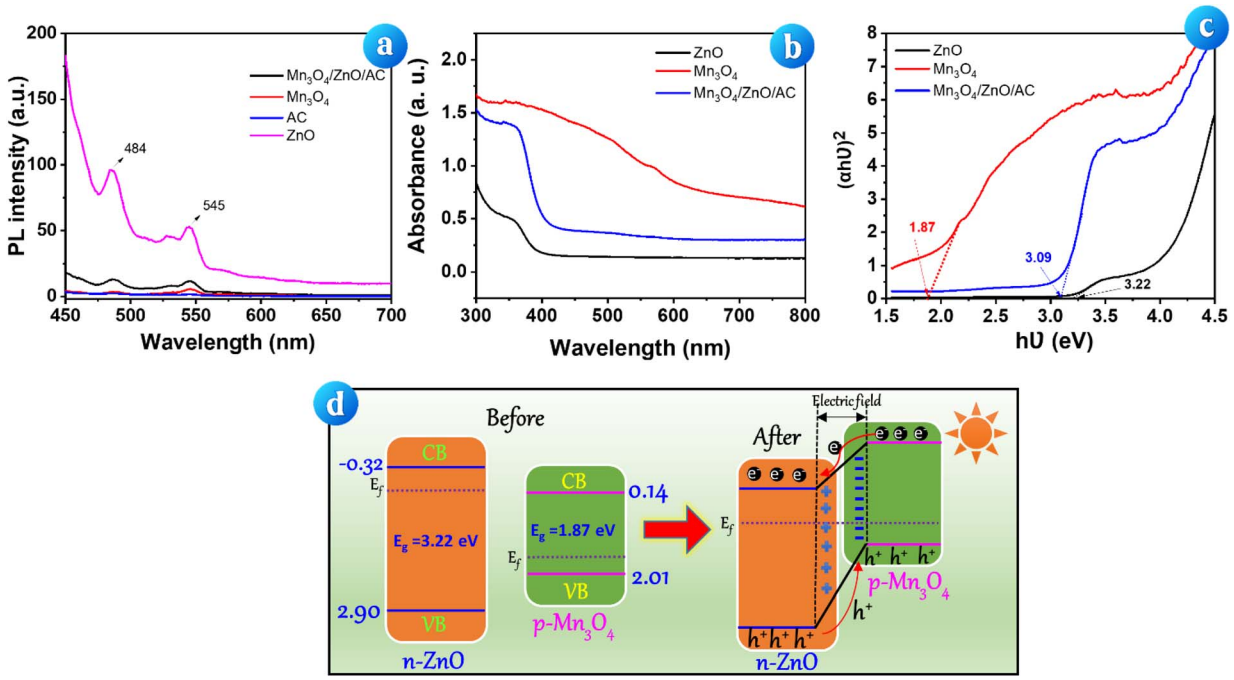

Fig. 4 UV-absorbance spectrum (a) of ZnO, Mn_3O_4, and Mn_3O_4/ZnO/AC, along with their Tauc's energy band gap plots (b), PL emission spectra (c) of the prepared samples, (d) the energy band structure of Mn_3O_4 and ZnO before contact, the formation of the p–n junction, and the charge separation mechanism in the Mn_3O_4/ZnO heterostructure under visible light.

The analysis of bandgap energies is crucial as it directly influences the photocatalytic activity by determining the material's light absorption range. The DRS data (Fig. 4b) for ZnO, Mn_3O_4, and Mn_3O_4/ZnO/AC composite were analyzed to determine the bandgaps using the Tauc formula (eqn (5)):[23]

$$(\alpha h\nu)^n = A(h\nu - E_g) \quad (5)$$

where α is the absorption coefficient, $h\nu$ is the photon energy, A is a constant, and n is determined by the type of transition. The Tauc plot is illustrated in Fig. 4c.

Fig. 4b indicates an absorption edge for ZnO at around 390 nm, corresponding to a bandgap energy (E_g) of around 3.22 eV. Meanwhile Mn_3O_4 displays an absorption edge near 600 nm, suggesting a narrower bandgap of approximately 1.87 eV. A wider bandgap like that of ZnO is beneficial for UV-light-driven photocatalysis, while Mn_3O_4's narrower bandgap allows for visible light absorption, making the Mn_3O_4/ZnO/AC composite potentially active under both UV and visible light. The energy level alignment allows for efficient electron transfer from Mn_3O_4 to ZnO in the composite under visible light excitation, promoting effective charge separation and reducing electron–hole recombination. The incorporation of AC further enhances charge separation by facilitating electron transport, which is expected to improve the composite's photocatalytic activity in applications like pollutant degradation. This synergistic effect, derived from the complementary band structure and light absorption properties, underscores the importance of determining bandgap energies and energy levels for designing efficient photocatalytic materials.

To estimate the energy band positions of ZnO and Mn_3O_4, Mulliken's electronegativity theory was applied using the eqn (6) & (7):

$$E_{CB} = \chi - E_e - 0.5E_g \quad (6)$$

$$E_{VB} = E_{CB} + E_g \quad (7)$$

where χ represents the absolute electronegativity, E_e is the energy of free electrons on the hydrogen scale (approximately 4.5 eV), and E_g is the bandgap energy. For ZnO, with an electronegativity of 5.79 eV, the conduction band (CB) position is calculated to be around −0.32 eV, and the valence band (VB) at approximately 2.90 eV. For Mn_3O_4, with an estimated bandgap of 1.87 eV and an electronegativity of 5.57 eV,[24] the CB edge is approximately 0.14 eV, and the VB edge around 2.01 eV.

Fig. 4d depicts the energy band structure of Mn_3O_4 and ZnO before contact, the formation of the p–n junction, and the charge separation mechanism in the Mn_3O_4/ZnO heterostructure under visible light irradiation. Mn_3O_4, a p-type semiconductor, has its Fermi level positioned near the valence band, whereas ZnO, an n-type semiconductor, features a Fermi level closer to the conduction band.[25,26] When Mn_3O_4 and ZnO come into contact, they form a p–n junction. At this junction, electrons move from the n-ZnO region to the p-Mn_3O_4 region, causing a buildup of negative charges in p-Mn_3O_4 near the interface. At the same time, holes from p-Mn_3O_4 migrate into n-ZnO, creating a region with positive charges in n-ZnO close to the junction. Once the Fermi levels of Mn_3O_4 and ZnO balance, an internal electric field is created, pointing from n-ZnO to p-Mn_3O_4. This field prevents further movement of charges across

the junction. During this process, the energy levels of ZnO shift downward, while those of Mn_3O_4 shift upward to reach equilibrium. Under visible-light irradiation, Mn_3O_4 generates electron–hole pairs, which contribute to the photocatalytic activity.[27]

3.1.5. Textural properties. The textural characteristics of the samples were analyzed using BET nitrogen adsorption–desorption isotherms and BJH pore size distribution analysis, as illustrated in Fig. 5. These analyses provide insights into the specific surface area (S_{BET}), pore volume, and pore diameter of the materials (Table 1), which are critical factors in determining their suitability for catalytic and adsorption applications. The BET isotherms of the green microalgae-derived AC (Fig. 5a), ZnO/AC (Fig. 5c), and Mn_3O_4/ZnO/AC (Fig. 5e) all exhibit a type IV isotherm with H3 hysteresis loop, which is characteristic of mesoporous materials.[28] This type of isotherm is marked by a hysteresis loop, which is indicative of capillary condensation within the mesopores. The presence of this hysteresis loop confirms the mesoporous nature of the samples, particularly after the incorporation of ZnO and Mn_3O_4.

The green microalgae-derived AC exhibits a relatively low specific surface area of 8.04 $m^2\ g^{-1}$, with a pore volume of 0.011 $cm^3\ g^{-1}$ and an average pore diameter of 1.69 nm. This indicates a modest porosity, primarily consisting of micropores, which is consistent with the inherent structure of the microalgae. Notably, the specific surface area of our AC is comparable to that of the *Ulva lactuca*-derived biochar-sulfur reported in the literature, which has an S_{BET} of 6.26 $m^2\ g^{-1}$.[11] This similarity

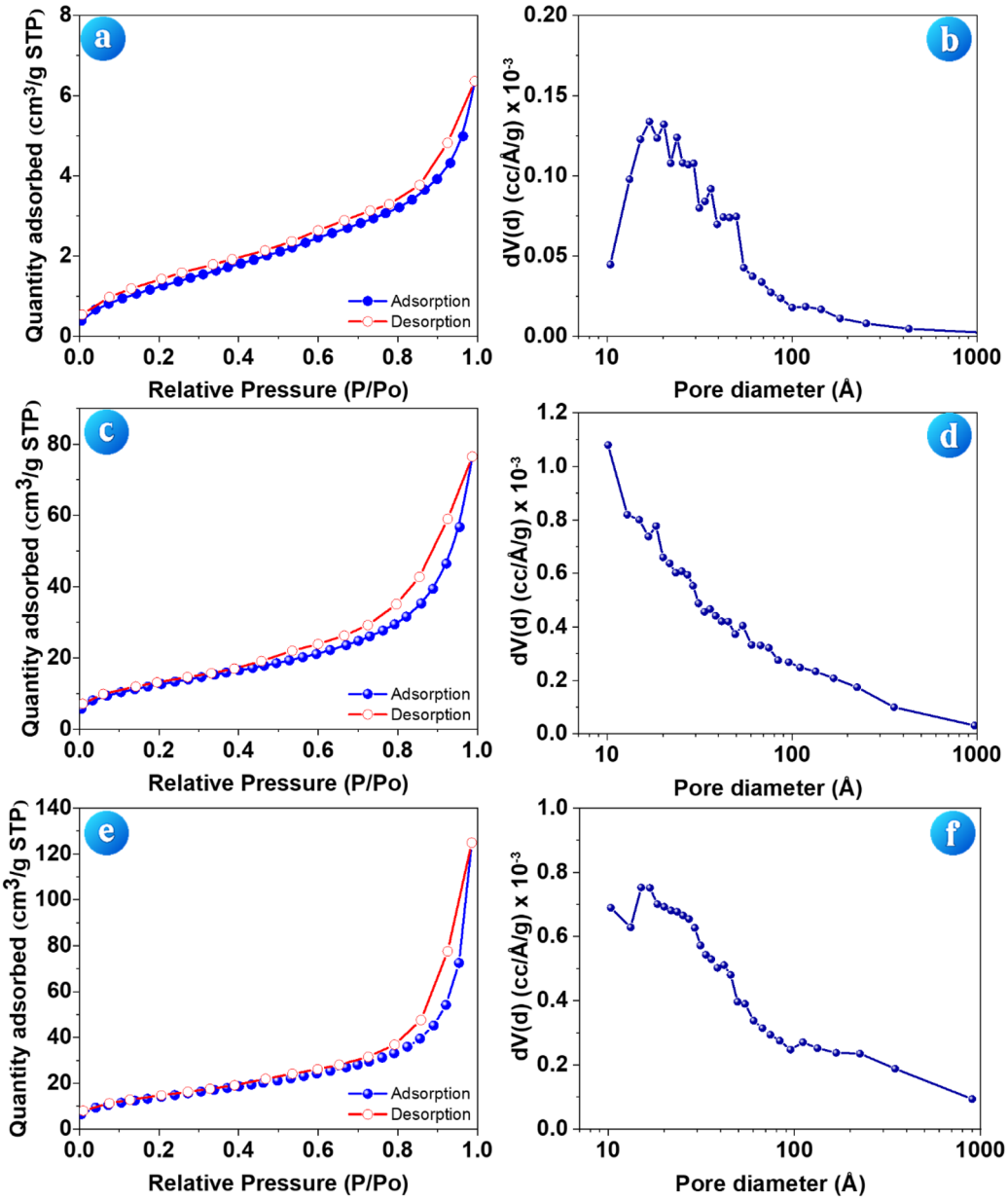

Fig. 5 BET nitrogen adsorption–desorption isotherms (a, c and e) and BJH pore size distribution curves (b, d and f) for green microalgae-derived AC (a and b), ZnO/AC (c and d), and Mn_3O_4/ZnO/AC (e and f).

Table 1 Textural parameters of the prepared samples

Sample	S_{BET} ($m^2\ g^{-1}$)	Pore volume ($cm^3\ g^{-1}$)	Pore diameter (nm)
AC	8.04	0.011	1.69
ZnO/AC	69.49	0.125	1.01
Mn_3O_4/ZnO/AC	75.70	0.199	1.50

suggests that the surface area of microalgae-derived carbons is relatively consistent across different species, underscoring the effectiveness of microalgae as a precursor for producing activated carbons with modest but functional porosity. Upon incorporation of ZnO onto the AC matrix, a significant enhancement in the textural properties is observed. The S_{BET} increases markedly to 69.49 $m^2\ g^{-1}$, along with a substantial rise in pore volume to 0.125 $cm^3\ g^{-1}$. Interestingly, the average pore diameter decreases to 1.01 nm, suggesting that ZnO nanoparticles contribute to a denser packing within the pore structure, which enhances the surface area by opening up more micropores or creating new mesopores. Further modification by introducing Mn_3O_4 into the ZnO/AC composite results in a further increase in the specific surface area to 75.70 $m^2\ g^{-1}$. The pore volume also increases to 0.199 $cm^3\ g^{-1}$, and the average pore diameter expands to 1.50 nm. This increase in both surface area and pore volume can be attributed to the additional porosity introduced by Mn_3O_4, which likely generates new mesopores or enlarges existing ones, thus optimizing the material for catalytic applications where a high surface area and accessible pore structure are essential. These findings indicate that the sequential modification of AC with ZnO and Mn_3O_4 significantly enhances its textural properties, making the Mn_3O_4/ZnO/AC composite a promising candidate for applications that require high surface areas and well-distributed porosity, such as in catalysis and adsorption processes.

3.2. Photocatalytic evolution

The photocatalytic activity of the Mn_3O_4/ZnO/AC composite for the degradation of RhB under visible light irradiation was investigated and compared to that of individual and binary catalyst systems, including ZnO, Mn_3O_4, Mn_3O_4/AC, and ZnO/AC. Fig. 6a displays the UV-vis spectra of the RhB solution at different intervals during the photocatalytic reaction with the Mn_3O_4/ZnO/AC composite. The intensity of the absorption peak at 553 nm, characteristic of RhB, gradually decreased over time, indicating a progressive degradation of the dye. A nearly complete degradation was observed after 420 min of reaction, demonstrating the high photocatalytic efficiency of the Mn_3O_4/ZnO/AC composite.

To further understand the efficiency of each catalyst, Fig. 6b compares the photocatalytic degradation profiles of RhB using various catalysts. A control experiment without any catalyst (photolysis) showed that only 4.23% of RhB was degraded after 7 h of illumination, highlighting the dye's stability under light and confirming that the observed RhB degradation in the presence of catalysts is primarily due to their photocatalytic activity.[29] Before the photocatalytic tests, the adsorption capacity of each material in the dark was evaluated. After 60 min, adsorption equilibrium was reached, with the adsorption capacity following this trend: ZnO (3.60%) < Mn_3O_4 (3.66%) < Mn_3O_4/AC (5.11%) < ZnO/AC (20.40%) < Mn_3O_4/ZnO/AC (22.96%). The Mn_3O_4/ZnO/AC composite demonstrated the

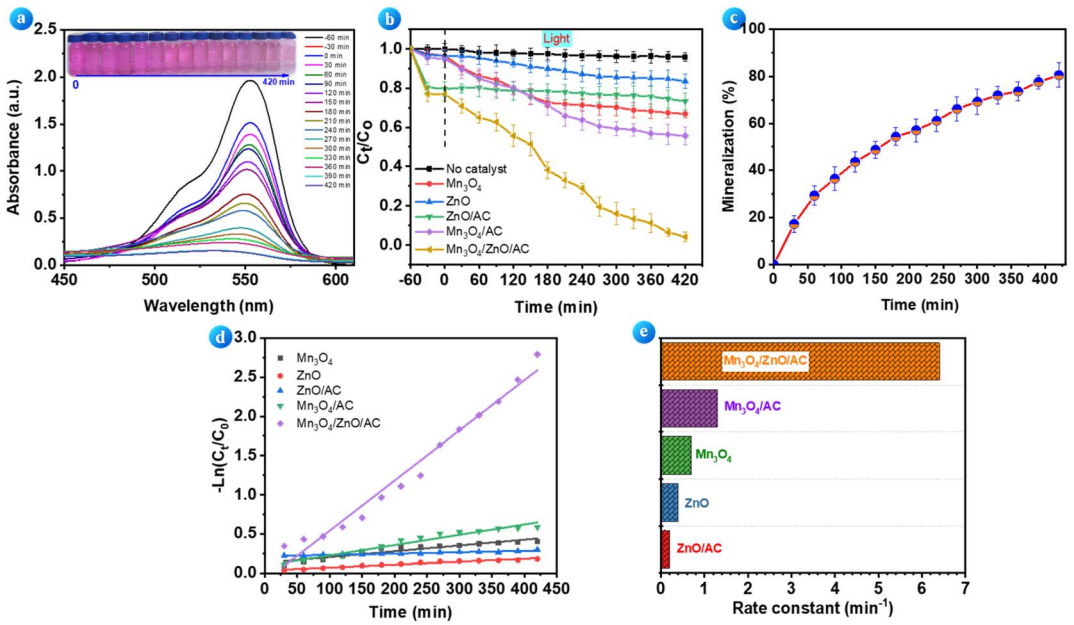

Fig. 6 (a) UV-vis absorption spectra of RhB solution over time during photocatalytic degradation using Mn_3O_4/ZnO/AC composite; (b) photocatalytic degradation profiles of RhB with various catalysts under visible light irradiation; (c) mineralization efficiency of RhB over time based on TOC measurements; (d) kinetic plots of RhB degradation based on a pseudo-first-order reaction model; (e) comparison of rate constants for RhB degradation with different catalysts. Experimental condition: [RhB] = 10 mg L^{-1}, catalyst dosage of 2 g L^{-1}, pH of 7, temperature of 25 °C.

highest adsorption capacity, likely due to its larger BET surface area and the presence of AC, which is known for its excellent adsorption properties. Although the total adsorption capacity of the catalysts remained below 25%, the significant enhancement in adsorption due to AC was evident.

When exposed to light, the photocatalytic performance of the catalysts differed significantly. Among the tested materials, the Mn_3O_4/ZnO/AC composite exhibited the highest photocatalytic efficiency, achieving 95.85% degradation of RhB within 420 min of illumination. In contrast, ZnO and Mn_3O_4 alone showed significantly lower degradation efficiencies of 16.46% and 33.17%, respectively. The poor performance of these single-component systems can be attributed to their wide band gaps, limiting their activity under visible light.[8,30] ZnO/AC showed only a slight improvement in RhB degradation under light compared to its dark adsorption capacity, with an additional 6% degradation. This suggests that ZnO/AC has limited photocatalytic activity, possibly due to its strong adsorption, which may prevent sufficient light from reaching the catalytic sites.[31] Meanwhile, Mn_3O_4/AC exhibited a much greater photocatalytic effect, degrading nearly 40% of RhB under light, highlighting its superior photocatalytic performance compared to ZnO/AC. Both binary systems, ZnO/AC and Mn_3O_4/AC, outperformed their single-component counterparts in RhB degradation. However, the photocatalytic efficiency of these binary catalysts was still lower than that of the Mn_3O_4/ZnO/AC composite. The remarkable enhancement in the Mn_3O_4/ZnO/AC system can be attributed to the synergistic interactions between Mn_3O_4, ZnO, and AC, which likely promoted more efficient charge separation, improved light absorption, and increased RhB adsorption onto the catalytic surface.

In comparison to other catalysts presented in the literature (Table 2), the Mn_3O_4/ZnO/AC composite, despite a relatively longer degradation time of 7 h, still demonstrated a respectable RhB removal efficiency of 95.85%. For instance, ZnO NPs showed a similar efficiency of 95% within 70 min, and Bi_2MoO_6/g-C_3N_4 achieved 94.6% removal in 3 h under UV-light. Although these systems exhibit faster degradation rates, it's important to note that the Mn_3O_4/ZnO/AC composite operates under visible light, which is more relevant for practical environmental applications where UV light sources are less common. Other systems, such as the ZnO/MIL-101(Fe)[A], CuO/CdO, and HA-Ag_3PO_4 composites, reached higher efficiencies (97.1%, 99.5% and 99.87%, respectively), but they rely on expensive or less abundant materials, which may limit their large-scale applications. The Mn_3O_4/ZnO/AC composite's performance, combined with its ease of synthesis and operation under visible light, remains competitive, especially in applications where visible light activation is crucial.

To evaluate the extent of contaminant mineralization, TOC measurements were performed, providing a comprehensive assessment of the photocatalyst's ability to fully degrade RhB into inorganic products like CO_2 and H_2O. As depicted in Fig. 6c, the mineralization efficiency progressively increased with reaction time, demonstrating the composite's strong photocatalytic performance. Initially, the mineralization rate was modest (~17%) due to the predominance of RhB adsorption and the gradual initiation of photocatalytic reactions. However, as the reaction proceeded, the mineralization rate accelerated. This enhancement was attributed to the generation of reactive species, such as hydroxyl radicals ($^{\bullet}OH$) and superoxide anions ($O_2^{\bullet-}$), which effectively broke down the dye's aromatic structure into smaller intermediates and eventually converted them into inorganic end-products. After 420 min of visible light irradiation, the mineralization efficiency reached an impressive 80.56%. This result highlights the Mn_3O_4/ZnO/AC composite's capability to degrade RhB beyond mere decolorization, ensuring the removal of potentially toxic intermediates. Such a high level of mineralization underscores the photocatalyst's potential for practical wastewater treatment applications, where comprehensive pollutant removal is crucial for environmental safety.

The kinetic analysis of RhB degradation, as shown in Fig. 6d, was conducted using a pseudo-first-order model, which is commonly used to describe the photocatalytic degradation of organic pollutants. The model is represented by the linear relationship of $-\ln(C_t/C_0)$ *versus* time, where C_0 is the initial concentration of RhB, and C_t is the concentration at a given time. From the slope of the linear plots, the rate constant (k, min^{-1}) for each catalyst was determined, offering a quantitative measure of their photocatalytic performance.[29] The Mn_3O_4/ZnO/AC composite demonstrated the highest rate constant ($k = 6.4 \times 10^{-3}$ min^{-1}), which was significantly higher than that of the Mn_3O_4/AC ($k = 1.3 \times 10^{-3}$ min^{-1}) and ZnO/AC ($k = 0.2 \times 10^{-3}$ min^{-1}) binary systems, as illustrated in Fig. 6e. Meanwhile, the individual catalysts, ZnO and Mn_3O_4, exhibited

Table 2 Photodegradation efficiency of RhB over different catalyst systems

Materials	Conditions	Removal efficiency (%)	Ref.
ZnO NPs	[RhB] = 25 mg L^{-1}, pH 7, catalyst dosage of 2 g L^{-1}, UV light, 70 min	95.0	32
ZnO/$NiFe_2O_4$	[RhB] = 10 mg L^{-1}, catalyst dosage of 0.75 g L^{-1}, sunlight, 3 h	95.7	33
ZnO/MIL-101(Fe)[A]	[RhB] = 10 mg L^{-1}, catalyst dosage of 0.5 g L^{-1}, vis. light, 5 h	97.1	34
Cu–ZnO/rGO	[RhB] = 5 mg L^{-1}, catalyst dosage of 2 g L^{-1}, sunlight, 7 h	95.0	35
CuO/CdO	[RhB] = 20 mg L^{-1}, pH 7, catalyst dosage of 0.8 g L^{-1}, vis. light, 90 min	99.5	23
HA-Ag_3PO_4	[RhB] = 20 mg L^{-1}, catalyst dosage of 1.0 g L^{-1}, vis. light, 2 h	99.87	36
TiO_2/$CuFe_2O_4$	[RhB] = 5 mg L^{-1}, pH 10, catalyst dosage of 1 g L^{-1}, UV-vis. light, 2.5 h	91.2	29
Bi_2MoO_6/g-C_3N_4	[RhB] = 1 mg L^{-1}, catalyst dosage of 1 g L^{-1}, pH = 6.9, UV light, 3 h	94.6	37
Mn_3O_4/ZnO/AC	[RhB] = 10 mg L^{-1}, pH 7, catalyst dosage of 2 g L^{-1}, vis. light, 7 h	95.85	This study

low rate constants of 0.4×10^{-3} min^{-1} and 0.7×10^{-3} min^{-1}, respectively, further underscoring the synergistic effect observed in the ternary Mn_3O_4/ZnO/AC composite.

The superior kinetic performance of the Mn_3O_4/ZnO/AC composite can be attributed to several key factors. First, the presence of AC significantly increases the overall surface area, thereby enhancing the adsorption of RhB molecules and bringing them closer to the catalytic active sites. This improved adsorption, combined with the excellent light absorption properties of AC, allows for more efficient utilization of the visible light spectrum. Additionally, the heterojunction formed between Mn_3O_4 and ZnO is known to facilitate better charge separation, effectively suppressing electron–hole recombination, which is one of the primary factors limiting photocatalytic efficiency in semiconductor-based systems. Moreover, the hierarchical structure of the Mn_3O_4/ZnO/AC composite may promote more effective diffusion of RhB molecules to the catalytic sites, further enhancing the overall degradation rate. This suggests that the integration of AC with both Mn_3O_4 and ZnO not only improves adsorption but also significantly boosts the photocatalytic activity through enhanced light-harvesting and charge–transfer properties. In terms of practical implications, the high rate constant of the Mn_3O_4/ZnO/AC composite suggests its potential as an effective photocatalyst for the degradation of organic dyes and possibly other pollutants under visible light irradiation. This observation is consistent with other studies that report enhanced photocatalytic activity in multi-component systems, where a combination of semiconductor materials and a carbon-based support leads to superior performance in environmental remediation applications.[10,28,38]

3.3. Effect of the operating parameters

3.3.1. Effect of pH. The pH of the reaction environment plays a critical role in influencing the photocatalytic activity of Mn_3O_4/ZnO/AC, as it affects both the surface charge of the catalyst and the ionization state of the target pollutant. The isoelectric point (pH_{pzc}) of Mn_3O_4/ZnO/AC was determined to be 7.8 using the drift pH method. This means that at pH values lower than 7.8, the surface of the catalyst is positively charged, while at pH values higher than 7.8, the surface becomes negatively charged. To explore the impact of pH on the degradation efficiency of RhB, the photocatalytic experiments were conducted at different pH values (3, 5, 7, 9, and 11), with the results shown in Fig. 7a. The degradation efficiency exhibits a clear dependence on pH, with the optimal performance observed at neutral pH (pH 7), where approximately 95.85% of RhB was degraded after 7 h. At pH 7, the surface charge of Mn_3O_4/ZnO/AC is near neutral, allowing for the most favorable interaction between the catalyst and RhB molecules. The neutral environment promotes optimal adsorption of RhB on the catalyst surface, without significant electrostatic repulsion. Furthermore, at this pH, the generation of hydroxyl radicals ($^{\bullet}OH$) is efficient, leading to enhanced degradation. Similar results were observed when RhB was degraded by Bi_2MoO_6/g-C_3N_4 (ref. 37) and CuO/CdO.[23]

At more acidic conditions (pH 3 and 5), the degradation efficiency significantly decreases, with only 27.91% removal at pH 3 and 66.74% at pH 5. The reduced activity at low pH can be attributed to the protonation of the catalyst's surface, which, while increasing the positive charge density, may lead to electrostatic repulsion with the cationic form of RhB. This repulsion reduces the adsorption of RhB on the catalyst, lowering the degradation efficiency. Additionally, under strongly acidic conditions, excess H^+ ions can interfere with the formation of reactive oxygen species, further hindering the photocatalytic process. At pH values above 7.8 (the isoelectric point of Mn_3O_4/ZnO/AC), the surface of the catalyst becomes negatively charged. Meanwhile, RhB remains positively charged (RhB^+) in mildly basic environments. This creates an electrostatic attraction between the catalyst and RhB^+, which may lead to strong adsorption of RhB onto the catalyst surface. While this could initially seem beneficial, it can, in fact, hinder the photocatalytic efficiency by excessively blocking the active sites, limiting light penetration and preventing effective generation of reactive species. Moreover, at very high pH ($\geq$9), RhB may undergo partial deprotonation, leading to the formation of carboxylate groups ($-COO^-$). This introduces electrostatic repulsion between the carboxylate anions and the negatively charged catalyst surface, further reducing RhB's adsorption and decreasing the photocatalytic degradation efficiency.[39] Another possible factor contributing to the reduced performance at high pH is the transformation of ZnO and Mn_3O_4 into their respective hydroxide complexes, such as $Zn(OH)_{2-4}$ and $Mn(OH)_{2-4}$.[40] These complexes are less effective as photocatalysts compared to the oxides, further limiting the system's overall catalytic activity. Thus, the decrease in photocatalytic activity at pH values above 9 is likely due to a combination of strong adsorption that limits light absorption, electrostatic repulsion between RhB and the catalyst, and the formation of inactive hydroxide species.

3.3.2. Effect of catalyst dosage. The selection of an optimal catalyst dosage is essential not only for maximizing photocatalytic efficiency but also for ensuring cost-effectiveness by minimizing the amount of material used without compromising performance. In this study, the impact of different Mn_3O_4/ZnO/AC dosages (ranging from 1.0 to 2.5 g L^{-1}) on the degradation efficiency of RhB was evaluated. The results are shown in Fig. 7b, which highlights the relationship between the catalyst amount and the degradation rate.

Initially, the photocatalytic degradation efficiency increased markedly as the catalyst dosage was raised from 1.0 g L^{-1} to 2.0 g L^{-1}. At 1.0 g L^{-1}, the degradation efficiency was 77.5%, which increased significantly to 89.1% at 1.5 g L^{-1} and reached the maximum of 95.85% at 2.0 g L^{-1}. This improvement can be attributed to the increased availability of active sites on the catalyst surface, allowing for more photon absorption and enhanced generation of reactive species responsible for RhB degradation.[29] However, a further increase in catalyst dosage beyond 2.0 g L^{-1} did not result in improved performance. In fact, the degradation efficiency slightly decreased to 92.5% at 2.5 g L^{-1}. This reduction in efficiency at higher catalyst dosages can be explained by the screening effect: when the catalyst

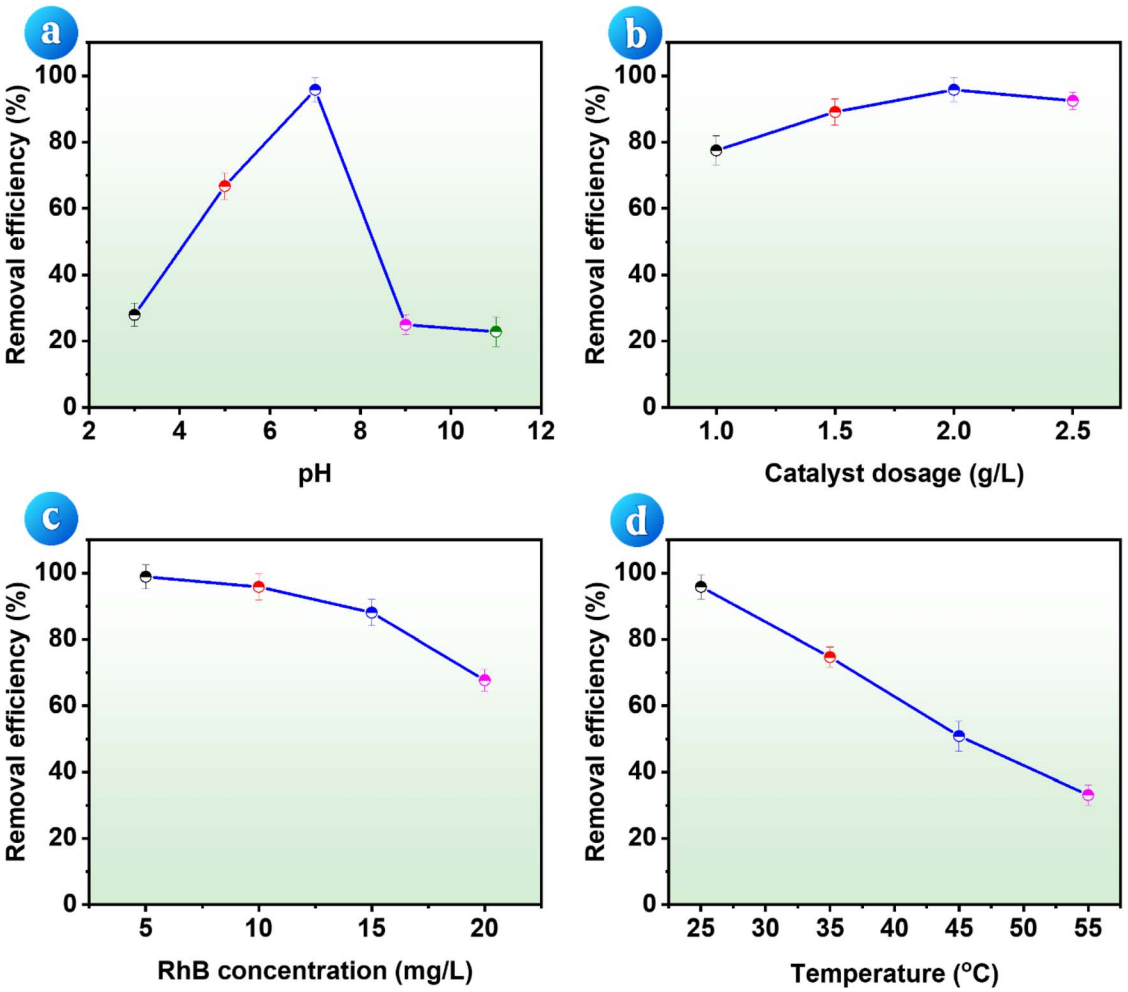

Fig. 7 Effects of the operating parameters on the photodegradation of RhB by the Mn_3O_4/ZnO/AC composite: (a) pH, (b) catalyst dosage, (c) dye concentration, and (d) temperature. Fixed experimental conditions: [RhB] = 10 mg L^{-1}, catalyst dosage of 2 g L^{-1}, pH of 7, temperature of 25 °C.

concentration is too high, excess catalyst particles can aggregate or scatter the incident light, reducing the overall light penetration through the suspension. As a result, fewer photons reach the active sites, and the rate of reactive species generation is diminished. Additionally, high catalyst concentrations may lead to excessive adsorption of RhB on the surface, further limiting its photocatalytic breakdown.[41] Therefore, while increasing catalyst dosage enhances the degradation up to an optimal point (2.0 g L^{-1}), higher amounts may negatively impact the process due to light shielding and particle agglomeration effects. Hence, an optimal balance of catalyst dosage must be maintained to maximize the photocatalytic activity of Mn_3O_4/ZnO/AC.

3.3.3. Effect of RhB concentration. Careful control of RhB concentration is essential for maintaining high degradation efficiency and optimizing the performance of the catalyst system. Therefore, the effect of initial RhB concentration on the catalytic activity of the Mn_3O_4/ZnO/AC composite was investigated, and the results are presented in Fig. 7c. The findings reveal that as the initial concentration of RhB increases, the removal efficiency significantly decreases, highlighting the crucial role that substrate availability plays in the photocatalytic process. At lower RhB concentrations (5 mg L^{-1}), the catalyst exhibited an impressive removal efficiency of 98.89%, suggesting an optimal interaction between dye molecules and the active sites on the catalyst surface. This suggests that at low concentrations, there is an abundance of active sites on the Mn_3O_4/ZnO/AC surface, allowing for efficient adsorption and degradation of RhB molecules.

As the RhB concentration increased to 10 and 15 mg L^{-1}, the removal efficiency dropped slightly to 95.85% and 88.07%, respectively. This reduction can be attributed to the saturation of active sites on the Mn_3O_4/ZnO/AC surface, leading to decreased accessibility for the dye molecules.[42] At higher RhB concentrations, competition for available active sites intensifies, resulting in a lower photocatalytic efficiency. Furthermore, the higher concentration of RhB may limit the penetration of light into the solution due to increased absorption, which in turn reduces the generation of reactive oxygen species required for the degradation process.[29] When the RhB concentration reached 20 mg L^{-1}, a more significant decline in removal efficiency was observed, dropping to 67.74%. This pronounced decrease can be explained by the excessive amount of dye in the system, which not only overwhelms the catalyst's

surface but also causes a shielding effect that inhibits effective light absorption. The high concentration of RhB molecules can absorb a significant portion of the incident light, reducing the energy available for the catalyst to initiate the photocatalytic reactions. Moreover, the increased number of RhB molecules leads to higher competition for photon absorption, further slowing the degradation rate.[43] Thus, at higher concentrations of RhB, the catalytic efficiency of Mn_3O_4/ZnO/AC is hindered by both the limited availability of active sites and the obstruction of light, emphasizing the importance of optimizing dye concentrations in practical applications. In this study, 10 mg L^{-1} was selected as the representative RhB concentration for further experiments because it provides a balanced assessment of catalytic performance. At lower concentrations (*e.g.*, 5 mg L^{-1}), nearly complete removal (~98.89%) was achieved, making it difficult to observe significant variations in degradation rates and reaction kinetics. Conversely, at higher concentrations (≥15 mg L^{-1}), the degradation efficiency decreased substantially due to active site saturation and light shielding effects. Thus, 10 mg L^{-1} serves as an optimal midpoint, allowing for both sufficient degradation efficiency (~95.85%) and measurable catalytic differences under varying conditions.

3.3.4. Effect of temperature. Temperature plays a crucial role in determining the photocatalytic efficiency, as it directly influences the kinetics of the degradation process. To assess the effect of temperature on the photocatalytic degradation of RhB, experiments were conducted at four different temperatures (25 °C, 35 °C, 45 °C, and 55 °C), and the corresponding removal efficiencies are depicted in Fig. 7d. As shown in Fig. 7d, the removal efficiency decreased significantly with increasing temperature. At 25 °C, the catalyst exhibited the highest removal efficiency of 95.85%, indicating optimal conditions for the photocatalytic process. However, as the temperature increased, the removal efficiency dropped to 74.72% at 35 °C, 50.85% at 45 °C, and further down to 33.12% at 55 °C. This decline suggests that higher temperatures may hinder the photocatalytic activity. One possible explanation for this trend is the reduced adsorption of RhB onto the Mn_3O_4/ZnO/AC composite surface at elevated temperatures. At higher temperatures, desorption of RhB molecules is favored over adsorption, which is a critical step in the photocatalytic process. Additionally, the increased temperature may reduce the generation of reactive oxygen species, which are essential for breaking down RhB molecules. This phenomenon may be further influenced by the fact that rising temperatures in aqueous solutions lead to a decrease in dissolved molecular oxygen, suggesting a potential interdependence between temperature and oxygen availability. Since dissolved oxygen is crucial for the formation of ROS, the reduced oxygen levels at higher temperatures likely contribute to the diminished photocatalytic activity. This effect could also be related to the decomposition of intermediate products, leading to a decline in overall degradation efficiency.[44] The rate constants of the degradation process at different temperatures were calculated using the pseudo-first-order kinetic model, and the corresponding values are listed in the Table 3. A clear decrease in the rate constant is observed as the temperature rises, further confirming the negative impact of increased temperature on the catalytic activity.

From a practical application perspective, the significant decline in photocatalytic efficiency at elevated temperatures poses challenges for real-world deployment, especially in outdoor or industrial wastewater treatment systems where temperature fluctuations are common. However, this temperature-dependent behavior also presents certain advantages. The catalyst maintains high efficiency within the temperature range commonly found in natural and industrial wastewater settings (25–35 °C), reducing the need for external thermal regulation. Additionally, operation at lower temperatures may help preserve the structural integrity of the catalyst, preventing thermal degradation and extending its operational lifespan. These findings suggest that while improvements in thermal stability could enhance large-scale applicability, Mn_3O_4/ZnO/AC remains a promising material for moderate-temperature environments, where its efficiency and durability can be maximized.

The activation energy (E_a) and thermodynamic parameters such as enthalpy (ΔH), entropy (ΔS), and Gibbs free energy (ΔG) were also calculated (using eqn (8)–(11) (ref. 45)) to better understand the effect of temperature on the reaction mechanism.

$$\ln k = \ln A - \frac{E_a}{RT} \tag{8}$$

$$\Delta H = E_a - RT \tag{9}$$

$$\ln \quad = \quad - \frac{\Delta H}{RT} + \frac{\Delta S}{R} + \ln \frac{k_B}{h} \tag{10}$$

$$\Delta G = \Delta H - T\Delta S \tag{11}$$

where k (min^{-1}) represents the rate constant, A is the pre-exponential factor, E_a denotes the activation energy, R (8.314 J mol^{-1} K^{-1}) is the universal gas constant, T (K) is the absolute temperature, k_B is the Boltzmann constant, and h is Planck's constant.

Table 3 Thermodynamic parameters for RhB photodegradation by Mn_3O_4/ZnO/AC

T (°C)	Rate constant (min^{-1})	R^2	E_a (kJ mol^{-1})	ΔH (kJ mol^{-1})	ΔS (J mol^{-1} K^{-1})	ΔG (kJ mol^{-1})
25	0.0064	0.974	−45.88	−48.36	−449.03	85.45
35	0.0025	0.952		−48.44	−444.30	88.41
45	0.0014	0.943		−48.52	−439.89	91.36
55	0.0012	0.978		−48.61	−435.74	94.32

The results of the thermodynamic parameters are presented in Table 3. The activation energy was calculated as -45.88 kJ mol^{-1}, indicating an unusual reaction pathway where an increase in temperature results in a reduction in the reaction rate. The negative E_a observed in the degradation of RhB by the Mn_3O_4/ZnO/AC composite suggests a more complex reaction mechanism than typical elementary reactions. In simpler, single-step reactions, the activation energy is generally positive because increasing the temperature provides more molecules with enough energy to overcome the activation barrier, thus accelerating the reaction rate. However, in complex reactions involving intermediates, the situation changes. In this case, the reaction likely involves intermediates that play a crucial role in the overall degradation process. As temperature increases, the equilibrium between the reactants and these intermediates shifts, resulting in a decrease in the concentration of the intermediates. Even though the subsequent reaction step (involving the conversion of the intermediate to the final product) might proceed faster with increasing temperature due to a typical positive activation energy, the overall rate of RhB degradation can still decrease if the reduction in intermediate concentration outweighs the increased rate of the subsequent step. This interplay between the equilibrium shift and the reaction kinetics can create the appearance of a negative activation energy. The overall reaction slows down at higher temperatures not because the intrinsic activation energy is negative, but due to the diminished availability of key intermediates necessary for the reaction to proceed efficiently.[46] In the case of RhB degradation, as temperature rises, the Mn_3O_4/ZnO/AC photocatalyst may experience structural or surface changes that limit the formation or effectiveness of intermediates, further reducing the reaction rate.

The ΔH values, ranging from -48.36 to -48.61 kJ mol^{-1}, confirm that the degradation process is exothermic, releasing energy during the reaction. However, as the temperature increases, this energy release becomes less favorable, aligning with the observed decline in degradation efficiency at higher temperatures. The negative ΔS values, between -449.03 and -435.74 J mol^{-1} K^{-1}, suggest a decrease in disorder during the reaction, possibly due to the organized adsorption of RhB molecules onto the catalyst's surface, where they align in a structured manner, reducing the overall randomness of the system. Additionally, the positive Gibbs free energy values, ranging from 85.45 to 94.32 kJ mol^{-1}, indicate that the process is non-spontaneous without the presence of external energy, such as light.[47] While light drives the photocatalytic degradation, the increase in ΔG at higher temperatures suggests that more energy is required to sustain the reaction, further explaining the drop in efficiency at elevated temperatures.

3.4. Degradation pathway of RhB

Understanding the degradation pathway of organic pollutants is crucial for evaluating the efficiency and mechanisms of photocatalytic processes. The identification of intermediate products not only provides insights into the stepwise degradation but also ensures the potential environmental safety of the final products. Catalyzed by Mn_3O_4/ZnO/AC under visible light irradiation was examined through GC-MS analysis. The GC-MS spectrum (Fig. 8) revealed several intermediate compounds with different mass-to-charge ratios (m/z), providing insights into the stepwise degradation of RhB.

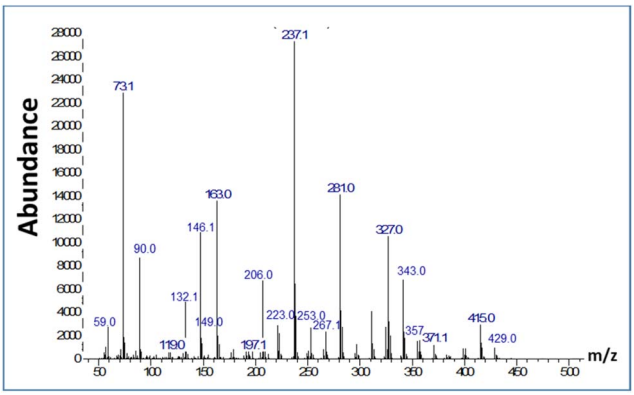

Fig. 8 GC-MS spectrum of photodegradation products of RhB over Mn_3O_4/ZnO/AC catalyst under visible light after 3 h. Experiment condition: [RhB] = 10 mg L^{-1}, pH 7, catalyst dosage of 2 g L^{-1}, 3 h.

Based on the GC-MS spectrum of photodegradation products (Fig. 8) and supported by previous studies,[48,49] the plausible degradation pathway of RhB under visible light irradiation in the Mn_3O_4/ZnO/AC catalytic system is proposed (Fig. 9). Initially, RhB (m/z = 443) undergoes dealkylation and decarboxylation reactions, leading to the formation of partially degraded intermediates with m/z values of 429, 415, 371, 357, 343, and 327. These reactions involve the cleavage of alkyl and carboxyl groups, gradually reducing the complexity of the RhB molecule. Following these initial reactions, the chromophore structure of RhB is broken down, producing smaller aromatic compounds with m/z values of 267, 281, 253, 237, 223, 209, 197, and 182. The cleavage of the chromophore is a key step, as it results in the decolorization of the dye, effectively diminishing its environmental impact.

Further degradation involves the ring-opening of aromatic intermediates into smaller organic molecules such as carboxylic acids, evidenced by the detection of compounds with m/z values of 163, 146, 132, 149, and 206. These reactions mark the transition from complex aromatic structures to simpler and more oxidized products. Ultimately, the degradation process culminates in mineralization, yielding end products such as CO_2, H_2O, NO_3^-, and NH_4^+. The presence of small organic acids, indicated by m/z values of 90, 88, 73, and 59, supports the complete breakdown of RhB into non-toxic compounds. This proposed degradation pathway highlights the high efficiency of the Mn_3O_4/ZnO/AC catalyst under visible light irradiation in decomposing RhB. These results not only validate the effectiveness of the catalyst but also provide a foundation for its application in real-world wastewater treatment systems.

3.5. Plausible mechanistic photodegradation

To understand the dominant reactive species responsible for RhB degradation over the Mn_3O_4/ZnO/AC composite, a series of

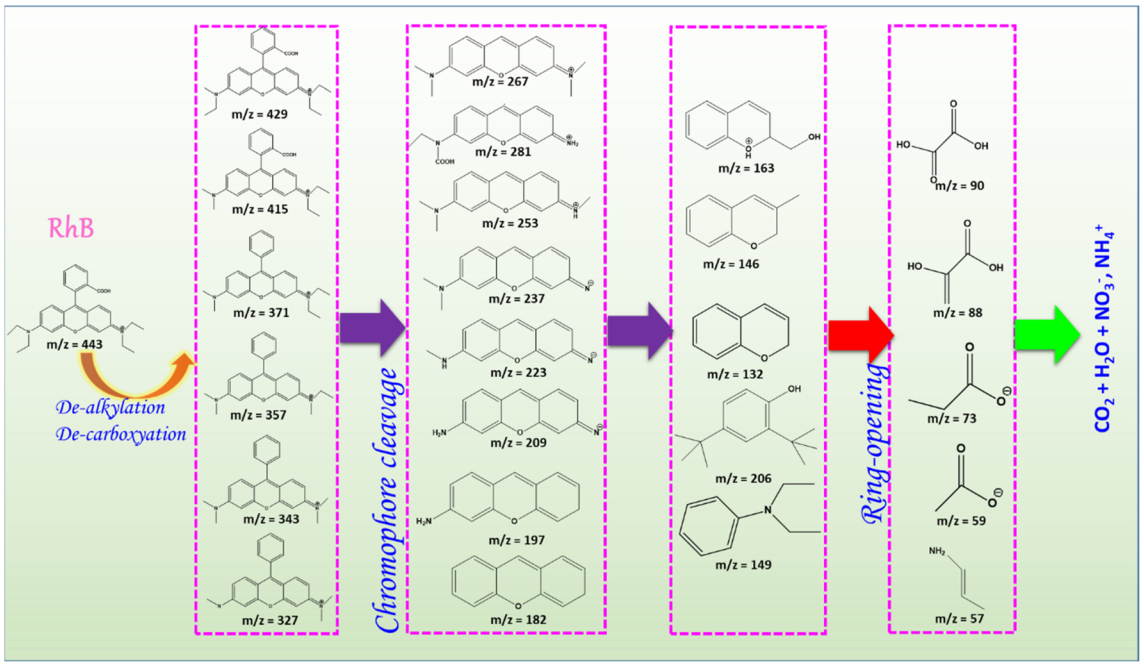

Fig. 9 Proposed degradation pathway of RhB over Mn_3O_4/ZnO/AC catalyst under visible light irradiation.

radical trapping experiments were conducted using various scavengers to inhibit specific reactive species. The results, displayed in Fig. 10a, indicate the impact of each scavenger on the photocatalytic degradation efficiency of RhB. In the blank test (without any scavenger), the composite achieved a degradation efficiency of 95.85%. However, the introduction of scavengers significantly altered this efficiency, suggesting the primary active species involved in the photodegradation mechanism. In the presence of *p*-BQ, a superoxide radicals ($O_2^{\bullet -}$) scavenger, the degradation efficiency dropped drastically to 21.43%, indicating that $O_2^{\bullet -}$ radicals play a crucial role in the degradation process. Similarly, the addition of IPA, a scavenger for hydroxyl radicals ($^{\bullet}OH$), led to a reduction in degradation efficiency to 29.06%, suggesting that $^{\bullet}OH$ radicals also significantly contribute to the photodegradation mechanism. When HCOONa was used as a hole (h^+) scavenger, the efficiency decreased to 66.49%, suggesting that h^+ also participates in the degradation process, though to a lesser extent than $O_2^{\bullet -}$ and $^{\bullet}OH$. In contrast, the presence of $K_2Cr_2O_7$, an electron scavenger, only slightly affected the efficiency, with a degradation rate of 91.85%, implying that photogenerated electrons play a minimal direct role in RhB degradation. These results reinforce the conclusion that $O_2^{\bullet -}$ and $^{\bullet}OH$ are the dominant reactive species driving the photocatalytic degradation mechanism on the Mn_3O_4/ZnO/AC composite.

Based on the scavenger test results and the proposed charge separation mechanism in the Mn_3O_4/ZnO heterostructure under visible light (Fig. 4d), the plausible mechanism for RhB

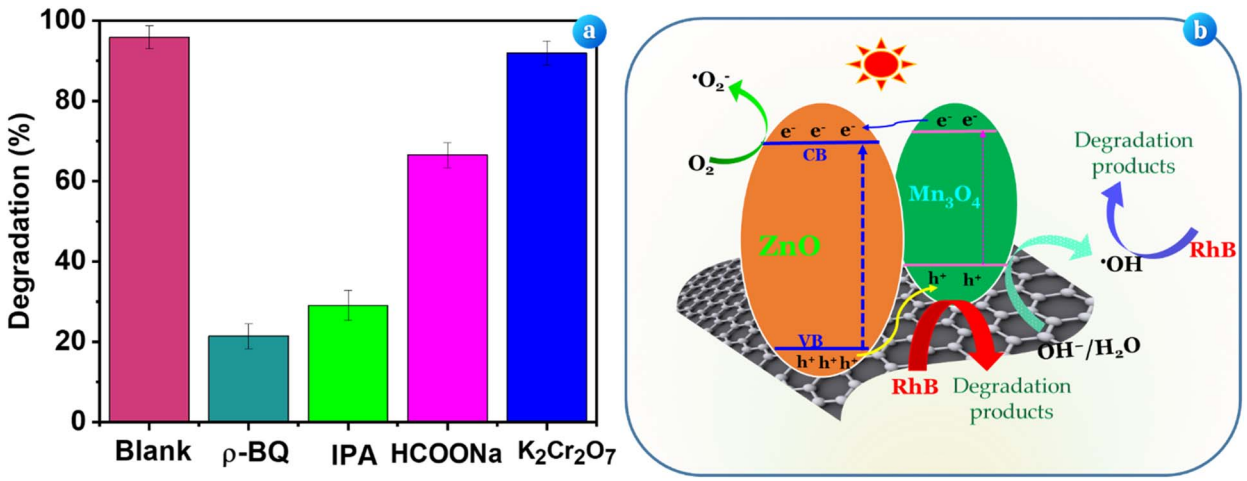

Fig. 10 (a) Effect of different scavengers on the RhB degradation, and (b) proposed photodegradation mechanism of RhB over the Mn_3O_4/ZnO/AC composite.

photodegradation over Mn_3O_4/ZnO/AC is illustrated in Fig. 10b. Upon irradiation, ZnO and Mn_3O_4 in the composite absorb light, promoting electrons from the valence band (VB) to the conduction band (CB) and generating electron–hole pairs (e^-/h^+) in both semiconductors (eqn (12) & (13)). The excited electrons in the CB of Mn_3O_4 migrate to the ZnO, which enhances the charge separation and reduces recombination (eqn (14)). The photogenerated electrons in the CB of ZnO react with O_2 molecules in the surrounding medium to produce $O_2^{\bullet-}$ (eqn (15)). Subsequently, $O_2^{\bullet-}$ can further react with H_2O to generate additional $^{\bullet}OH$ radicals, as shown in eqn (16). The holes in the VB of Mn_3O_4, on the other hand, oxidize H_2O or OH^- to generate $^{\bullet}OH$, as shown in the eqn (17) & (18). The generated ROS contribute to the degradation of RhB, as described in eqn (19). Therefore, the in-depth understanding of the degradation mechanism further enhances the potential for optimizing this photocatalyst for targeted pollutant degradation in diverse environmental settings.

$$ZnO + h\nu \rightarrow e_{(CB)}^- + h_{(VB)}^+ \quad (12)$$

$$Mn_3O_4 + h\nu \rightarrow e_{(CB)}^- + h_{(VB)}^+ \quad (13)$$

$$e_{Mn_3O_4(CB)}^- \rightarrow e_{ZnO(CB)}^- \quad (14)$$

$$e_{ZnO(CB)}^- + O_2 \rightarrow {}^{\bullet}O_2^- \quad (15)$$

$$^{\bullet}O_2^- + H_2O \rightarrow {}^{\bullet}OH + OH^- \quad (16)$$

$$h_{Mn_3O_4(VB)}^+ + OH^- \rightarrow {}^{\bullet}OH \quad (17)$$

$$h_{Mn_3O_4(VB)}^+ + H_2O \rightarrow {}^{\bullet}OH + H^+ \quad (18)$$

$$RhB + h^+/{}^{\bullet}OH/{}^{\bullet}O_2^- \rightarrow \text{degradation products} \quad (19)$$

3.6. Reusability and stability study

The stability and reusability of the Mn_3O_4/ZnO/AC catalyst were assessed over four successive photocatalytic degradation cycles of RhB under the same experimental conditions. As shown in Fig. 11a, the removal efficiency of the catalyst gradually decreased with each recycling run, starting at 95.85% in the first cycle and dropping to 91.9%, 89.1%, and 88.7% in the second, third, and fourth cycles, respectively. Although there was a slight decline in efficiency, the Mn_3O_4/ZnO/AC composite maintained over 88% degradation performance after four cycles, indicating strong reusability and stable catalytic activity. The decrease in photocatalytic efficiency can be attributed to minor surface fouling and possible loss of active sites over repeated cycles. However, this drop in performance was minimal, highlighting the robustness of the Mn_3O_4/ZnO/AC material in maintaining catalytic function even after multiple uses. Such stability is essential for practical applications where

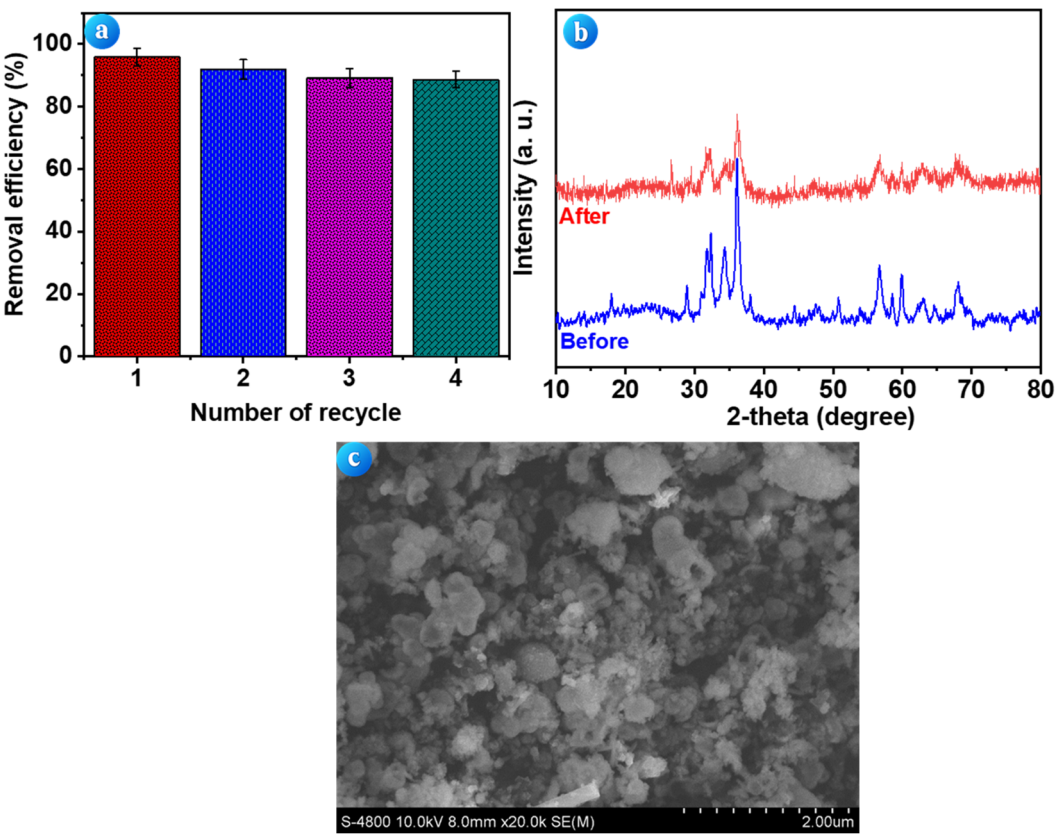

Fig. 11 Reusability and stability of Mn_3O_4/ZnO/AC catalyst: (a) photodegradation performance of Mn_3O_4/ZnO/AC over four consecutive cycles; (b) XRD patterns of Mn_3O_4/ZnO/AC before and after four cycles of reuse; (c) SEM images of Mn_3O_4/ZnO/AC after reuse. Experimental condition: [RhB] = 10 mg L^{-1}, catalyst dosage of 2 g L^{-1}, pH of 7, temperature of 25 °C.

long-term catalyst reusability is crucial for cost-effective and sustainable pollutant treatment.

The structural stability of the catalyst after reuse was confirmed by XRD analysis (Fig. 11b). The XRD patterns of the Mn_3O_4/ZnO/AC composite after four cycles showed no significant shifts in peak positions, suggesting that the crystal structure of the catalyst remained intact. This indicates that no significant phase transformation or structural degradation occurred during the photocatalytic process, further confirming the material's stability. Additionally, SEM images (Fig. 11c) of the Mn_3O_4/ZnO/AC composite after reuse revealed no major morphological changes. The catalyst retained its original surface texture and structure, without noticeable agglomeration or particle deterioration. These observations suggest that the Mn_3O_4/ZnO/AC composite exhibits excellent mechanical and structural stability, which is critical for maintaining consistent catalytic activity over extended operational cycles.

To further assess the stability and environmental safety of the Mn_3O_4/ZnO/AC composite, leaching experiments were conducted to quantify the release of Zn^{2+} and Mn^{2+} ions by ICP-MS during the photocatalytic degradation process. The results showed that the concentrations of leached Zn^{2+} and Mn^{2+} ions were 0.88 mg L^{-1} and 0.26 mg L^{-1}, respectively. These values were significantly below the maximum permissible limits set by the World Health Organization (WHO) for drinking water, which are 3 mg L^{-1} for Zn^{2+} and 0.4 mg L^{-1} for Mn^{2+}.[50] This indicates that the Mn_3O_4/ZnO/AC composite exhibits excellent chemical stability during operation, with minimal release of its constituent metal ions into the treated solution. The low leaching levels suggest that the material retains its structural integrity and minimizes the risk of secondary contamination, which is critical for the safe application of photocatalysts in real-world water treatment scenarios. Moreover, the observed ion concentrations were not only within safe limits but also reflected the robust bonding and interactions within the Mn_3O_4/ZnO/AC composite, which likely reduce the solubility of ZnO and Mn_3O_4 phases under photocatalytic conditions. An additional contributing factor is the neutral pH (pH 7) of the reaction environment, which helps stabilize the composite and prevents excessive ion dissolution. At pH 7, the solubility of metal oxides is minimized, reducing the likelihood of leaching and ensuring the material's chemical stability during the photocatalytic process. Overall, the reusability and stability tests confirm that the Mn_3O_4/ZnO/AC catalyst exhibits both high initial photocatalytic activity and outstanding durability, highlighting its potential for long-term environmental remediation applications.

4. Conclusions

This study successfully developed a Mn_3O_4/ZnO nanocomposite supported on microalgae-derived AC for efficient RhB degradation under visible light. The incorporation of Mn_3O_4 and ZnO into the AC matrix significantly enhanced photocatalytic efficiency by improving light absorption, charge carrier separation, and reactive oxygen species generation. Under optimal conditions ([RhB] = 10 mg L^{-1}, catalyst dosage = 2 g L^{-1}, pH = 7, T = 25 °C), the composite achieved over 95% RhB removal and 80.56% mineralization within 420 min of irradiation. Mechanistic investigations confirmed that hydroxyl radicals and superoxide radicals played dominant roles in RhB degradation. Stability tests revealed that the composite maintained 88.7% degradation efficiency after four cycles, with XRD and SEM analyses indicating minimal structural changes post-reuse. Furthermore, metal leaching tests confirmed the environmental compatibility of the composite, with Zn^{2+} (0.88 mg L^{-1}) and Mn^{2+} (0.26 mg L^{-1}) concentrations remaining well within WHO safety limits. These findings highlight the potential of Mn_3O_4/ZnO/AC as a cost-effective, sustainable photocatalyst for organic pollutant removal in wastewater treatment. The use of microalgae-derived AC aligns with green chemistry principles, transforming biomass waste into a value-added material. However, challenges remain, particularly regarding efficiency loss at elevated temperatures, which could limit large-scale outdoor applications. Future research should focus on enhancing thermal stability, integrating co-catalysts, and optimizing reactor design to improve practical performance and scalability.

Data availability

All data generated or analyzed during this study are included in this published article.

Author contributions

Conceptualization: Hoc Thang Nguyen, Van-Dat Doan, and Van Thuan Le; investigation and formal analysis: Hoc Thang Nguyen, Thi Lan Huong Nguyen, Anh-Tien Nguyen, and Quang-Hieu Tran; visualization and writing—original draft preparation: Hoc Thang Nguyen, Anh-Tien Nguyen, and Vy Anh Tran; writing—review and editing: Van-Dat Doan, Vy Anh Tran, and Van Thuan Le.

Conflicts of interest

There are no conflicts to declare.

References

1 C. Benbrika, H. Menasra, A. Kularkar, L. Smaili and A. Sbaihi, *J. Phys. Chem. Solids*, 2024, **184**, 111702.
2 A. Krishnan, A. Swarnalal, D. Das, M. Krishnan, V. S. Saji and S. M. A. Shibli, *J. Environ. Sci.*, 2024, **139**, 389–417.
3 F. Güell, A. Galdámez-Martínez, P. R. Martínez-Alanis, A. C. Catto, L. F. da Silva, V. R. Mastelaro, G. Santana and A. Dutt, *Mater. Adv.*, 2023, **4**, 3685–3707.
4 A. R. Bhapkar and S. Bhame, *J. Environ. Chem. Eng.*, 2024, **12**, 112553.
5 A. Ashpak Shaikh, M. Rajendra Patil, B. Sonu Jagdale and V. Ashok Adole, *Inorg. Chem. Commun.*, 2023, **151**, 110570.
6 P. Akhter, S. Nawaz, I. Shafiq, A. Nazir, S. Shafique, F. Jamil, Y.-K. Park and M. Hussain, *Mol. Catal.*, 2023, **535**, 112896.

7 P. Jansanthea, N. Inyai, W. Chomkitichai, J. Ketwaraporn, P. Ubolsook, C. Wansao, A. Wanaek, A. Wannawek, S. Kuimalee and P. Pookmanee, *Chemosphere*, 2024, **351**, 141212.
8 S. Khan, A. Hussain, K. He, B. Liu, Z. Imran, J. Ambreen, S. Hassan, M. Ahmad, S. S. Batool and C. Li, *J. Environ. Manage.*, 2021, **293**, 112854.
9 A. Gupta, Kajal, K. Ajravat, L. K. Brar, O. P. Pandey and P. Rajagopalan, *Mater. Chem. Phys.*, 2024, **313**, 128698.
10 T. Rungsawang, S. Krobthong, K. Paengpan, N. Kaewtrakulchai, K. Manatura, A. Eiad-Ua, C. Boonruang and S. Wongrerkdee, *Radiat. Phys. Chem.*, 2024, **223**, 111924.
11 A. G. M. Shoaib, H. T. Van, D. T. Tran, A. El Sikaily, M. A. Hassaan and A. El Nemr, *Sci. Rep.*, 2024, **14**, 11583.
12 Z. Djezzar, A. Aidi, H. Rehali, S. Ziad and T. Othmane, *RSC Adv.*, 2024, **14**, 5276–5289.
13 V. T. Le, T. K. N. Tran, N. K. Dang, V. D. Doan, V. A. Tran, Y. Vasseghian and T. M. Aminabhavi, *Chem. Eng. J.*, 2023, **474**, 145903.
14 I. K. Tetteh, I. Issahaku and A. Y. Tetteh, *Carbon Trends*, 2024, **14**, 100328.
15 J. Chen, K. Chu, S. Sun, H. Chen, B. Song, J. Wang, Z. Liu and L. Zhu, *J. Environ. Chem. Eng.*, 2023, **11**, 109230.
16 M. U. Dao, H. S. Le, H. Y. Hoang, V. A. Tran, V. D. Doan, T. T. N. Le, A. Sirotkin and V. T. Le, *Environ. Res.*, 2021, **198**, 110481.
17 V. T. Le, M. U. Dao, H. S. Le, D. L. Tran, V. D. Doan and H. T. Nguyen, *Environ. Technol.*, 2020, **41**, 2817–2832.
18 J. A. Lett, S. F. Alshahateet, I. Fatimah, R. P. Sivasankaran, A. K. Sibhatu, M.-V. Le and S. Sagadevan, *Top. Catal.*, 2023, **66**, 126–138.
19 M. L. de Peres, R. de A. Delucis, S. C. Amico and D. A. Gatto, *Nanomater. Nanotechnol.*, 2019, **9**, DOI: **10.1177/1847980419876201**.
20 X. Zhang, S. Luo, X. Wu, M. Feng, Y. Li, H. Han and W. Li, *Open Chem.*, 2021, **19**, 377–384.
21 D. Anbuselvan, S. Nilavazhagan, A. Santhanam, N. Chidhambaram, K. V. Gunavathy, T. Ahamad and S. M. Alshehri, *Phys. E*, 2021, **129**, 114665.
22 F. Mouzaia, D. Djouadi, A. Chelouche, L. Hammiche and T. Touam, *Arab J. Basic Appl. Sci.*, 2020, **27**, 423–430.
23 E. Arulkumar, S. Santhosh Shree and S. Thanikaikarasan, *Results Chem.*, 2023, **6**, 101169.
24 R. Rahimi, A. Mehrehjedy and S. Zargari, *Environ. Prog. Sustainable Energy*, 2017, **36**, 1439–1448.
25 L. Bigiani, D. Zappa, C. Maccato, A. Gasparotto, C. Sada, E. Comini and D. Barreca, *Nanomaterials*, 2020, **10**, 511.
26 K. D. Jayeola, D. S. Sipuka, T. I. Sebokolodi, O. V. Nkwachukwu, C. Muzenda, B. A. Koiki, J. O. Babalola, M. Zhou and O. A. Arotiba, *Chem. Eng. J.*, 2024, **479**, 147482.
27 J. Jiang, X. Zhang, P. Sun and L. Zhang, *J. Phys. Chem. C*, 2011, **115**, 20555–20564.
28 N. S. M. Sayed, A. S. A. Ahmed, M. H. Abdallah and G. A. Gouda, *Sci. Rep.*, 2024, **14**, 5384.
29 M. Osanloo, F. Khorasheh and A. Larimi, *J. Mol. Liq.*, 2024, **407**, 125242.
30 S. Abou Zeid and Y. Leprince-Wang, *Crystals*, 2024, **14**, 611.
31 V. T. Le, H. S. Le, V. A. Tran, L. Sang-Wha, V.-D. Doan, S.-W. Joo and Y. Vasseghian, *J. Ind. Eng. Chem.*, 2022, **115**, 345–354.
32 M. Lal, P. Sharma, L. Singh and C. Ram, *Results Eng.*, 2023, **17**, 100890.
33 Y. Stiadi, T. P. Wendari, Zilfa, Zulhadjri and Rahmayeni, *Environ. Eng. Res.*, 2022, **28**, 220074.
34 E. Amdeha and R. S. Mohamed, *Environ. Technol.*, 2021, **42**, 842–859.
35 P. G. Ramos, J. Espinoza, L. A. Sánchez and J. Rodriguez, *J. Alloys Compd.*, 2023, **966**, 171559.
36 I. Fatimah, R. Audita, G. Purwiandono, H. Hidayat, S. Sagadevan, W.-C. Oh and R. Doong, *Case Stud. Chem. Environ. Eng.*, 2024, **10**, 100797.
37 A. Masoud, M. A. Ahmed, F. Kühn and G. Bassioni, *Heliyon*, 2023, **9**, e22342.
38 V. T. Le, V. A. Tran, D. L. Tran, T. L. H. Nguyen and V.-D. Doan, *Chemosphere*, 2021, **270**, 129417.
39 F. Laatar, H. Moussa, H. Alem, L. Balan, E. Girot, G. Medjahdi, H. Ezzaouia and R. Schneider, *Beilstein J. Nanotechnol.*, 2017, **8**, 2741–2752.
40 A. T. Le, N. S. B. Samsuddin, S.-L. Chiam and S.-Y. Pung, *Bull. Mater. Sci.*, 2021, **44**, 5.
41 H. T. Nguyen, M. T. Truong, V.-D. Doan, T. L. H. Nguyen, V. H. Hoang, V. A. Tran, A.-T. Nguyen and V. T. Le, *Chem. Eng. Sci.*, 2024, **284**, 119487.
42 N. Mzimela, S. Tichapondwa and E. Chirwa, *RSC Adv.*, 2022, **12**, 34652–34659.
43 V. Doan, T. Thanh, N. Nguyen, H. Ai, L. Pham, T. Lan, H. Nguyen and V. T. Le, *J. Mol. Liq.*, 2024, **398**, 124261.
44 I. Groeneveld, M. Kanelli, F. Ariese and M. R. van Bommel, *Dyes Pigm.*, 2023, **210**, 110999.
45 V. T. Le, T. G. Duong, V. T. Le, T. L. Phan, T. L. Huong Nguyen, T. P. Chau and V.-D. Doan, *RSC Adv.*, 2021, **11**, 15438–15448.
46 Y.-H. Chiu, T.-F. Chang, C.-Y. Chen, M. Sone and Y.-J. Hsu, *Catalysts*, 2019, **9**, 430.
47 W. R. Abd-Ellatif, N. G. Mahmoud, A. A. Hashem, M. K. El-Aiashy, E. M. Ezzo and S. A. Mahmoud, *Environ. Technol. Innovation*, 2022, **27**, 102393.
48 Y. Ren, J. Wang, G. Qu, N. Ren, P. Lu, X. Chen, Z. Wang, Y. Yang and Y. Hu, *Sep. Purif. Technol.*, 2023, **314**, 123616.
49 N. A. Chopan and H.-T.-N. Chishti, *Mater. Today Chem.*, 2023, **32**, 101643.
50 M. Braga, R. Jaimes, W. Borysow, O. Gomes and W. Salcedo, *Sensors*, 2017, **17**, 1730.